Mechanisms of Lithospheric Dripping in Earth's Convecting Mantle: Implications for Tectonic Switching

Soham Banerjee[1], Dip Ghosh[2], Nibir Mandal[1*]

[1] Department of Geological Sciences, Jadavpur University, Kolkata, India
[2] Department of Geology, University of Calcutta, Kolkata, India
Corresponding author: nibir.mandal@jadavpuruniversity.in

Abstract

Gravity-driven dripping is a key recycling process of lithospheric materials into the underlying mantle reservoir. Here, we use 2D computational fluid dynamic (CFD) thermo-chemical simulations to unveil how such dripping process occurs by modulating the thermal convection in Earth's mantle. Our simulations incorporate the following variables: lithospheric buoyancy contrasts (B), metamorphic transformation of gabbroic crust into denser eclogite, mantle-to-lithosphere viscosity ratios, and mid-mantle phase transitions (olivine-wadsleyite, coesite-stishovite, and eclogitization). We recognize three distinct mechanisms; each of them gives rise to characteristic drip evolution that critically governs the layered versus whole-mantle convection dynamics. For buoyancy number $B \geq 0.29$, the initial viscosity ratio $M = 10$ and the density change due to eclogitization at mantle transition zone $\Delta\rho_{MM} \geq 150$ kg/m^3, lithospheric drips cluster into a train of superdrip structures (*Mechanism 1*), forming downwelling zones on a wavelength of 2800 km. The sinking superdrips eventually cross the 660 km barrier to penetrate lower mantle, fostering whole-mantle circulations. This drip mechanism undergoes a transition when $\Delta\rho_{MM}$ falls below 150 kg/m^3 and also when $0.29 > B > 0.16$ with $M = 10$, leading to stagnation of lithospheric drips at the 660 km boundary (*Mechanism 2*). We show that Mechanism 2 transforms the whole-mantle to layered convection styles, characterized by contrasting circulation patterns in the upper and lower mantle. In geodynamic conditions: $B \leq 0.16$ and $1000 \geq M \geq 10$, drips grow into asymmetric keel-like structures at the lithospheric base (*Mechanism 3*), occurring as proto-subduction analogues. This mechanism restores whole-mantle convective circulations, but with their wavelengths approximately 4200 km, significantly larger than that produced by Mechanism 1. Finally, based on observational datasets, our drip models provide a unified framework of drip-mediated lithospheric recycling mechanisms and stagnant-lid to modern plate tectonic transitions.

1. Introduction

During the Archaean Era, Earth's lithospheric tectonics was primarily driven by gravitational instabilities, specifically Rayleigh-Taylor (RT) instabilities at the base of the relatively cold, denser lithosphere that rested above the less dense, hotter asthenosphere(Beall et al., 2017). The gravitational forces in the dense lithosphere were strong enough to overcome the viscous resistance of the underlying asthenosphere, empowering the instabilities to grow at the lithosphere-asthenosphere boundary (LAB). Conrad and Molnar, (1997) showed that the wavelengths at which such instabilities grow at the fastest rates typically range from 100 to 200 km, which is approximately equal to the lithospheric thickness. The growing LAB instabilities eventually produced lithospheric drips (denser portions of the lithosphere) sinking into the mantle on a geological time scale (million years). Similar dynamics plays an important role in regions of lithospheric thickening, such as orogenic belts (Lei et al., 2019), where the dense lithospheric roots experience RT instabilities under strong lateral temperature gradients, resulting in removal of mantle lithosphere by convective flows (Bercovici & Girard, 2025; Houseman & Molnar, 1997). Previous studies suggested that the dripping process is sensitive to the stress-dependent viscous rheology of lithospheric materials that facilitates super-exponential growth of small perturbations into large descending blobs (Conrad & Molnar, 1997; Houseman & Molnar, 1997). Lev and Hager (2008), on the other hand, recognized pre-existing anisotropy in the lithosphere as another influential physical factor, significantly modifying the wavelength and the timing of instabilities. The presence of horizontal fabrics promotes faster growth of instabilities at large wavelengths, as compared to those developing under isotropic conditions. This anisotropic effect accounts for the formation of irregular lithospheric drips, and lateral offsets of instabilities from regions of maximum lithospheric thickness reported in literature (McMillan & Schoenbohm, 2023).

Gravity-driven drip processes have recently gained significant attention in solid earth sciences, as drip tectonics is thought to contribute to a wide range of geological phenomena, such as earthquake generations (Song & Klemperer, 2024), volcanism in orogenic systems, e.g., the central Appalachian Mountains (Long et al., 2021), depth anomalies in seismic tomography (Cox et al., 2016), and lithospheric basal erosion accompanied by topography changes due to isostatic adjustments (Andersen et al., 2024; Göğüş et al., 2017). In a recent study Houseman et al., (2025) have suggested that a compositionally buoyant mantle lithosphere, with its density deficit of 40 -78 kg/m^3 relative to asthenosphere, can experience

overturning by lithospheric dripping. This process leads to thinning of the layer and the injection of relatively hot materials into the Moho, without wholesale removal into the underlying asthenosphere. Their buoyancy-controlled drip model explains several key observations: post-collisional potassic volcanism, surface uplift (~600 m), a shift from N–S shortening to E–W extension and the preservation of deep (~200 km) fast seismic velocity anomalies beneath the Tibetan Plateau. Lithospheric dripping during the stagnant lid phase of Earth's tectonic history prior to the onset of plate tectonics is now thought to have been more complex than previously perceived (Foley, 2018; Gerya, 2019). This complexity, as suggested by Bercovici and Girard (2025), originates from coupling of Rayleigh–Taylor instability driven lithospheric dripping with viscous flexure under lateral compression by thermal stresses. On incorporation of two-phase grain damage, their analysis suggests that these drips evolve to form linear or arcuate weak zones, serving as possible precursors to proto-subduction or plate boundaries. Also, numerical model results suggest that lithospheric drips mostly contributed to the recycling process of dense, mafic lower crust into the mantle, particularly during the Archean era, when the Earth's mantle was significantly hotter than its present state(Johnson et al., 2014). The drip structures formed on varied scales under the influence of various factors, such as lithospheric thickness, density contrasts, and crustal strength (Gerya, 2014). The recycling of oceanic crusts eventually produced stable reservoirs in the mantle, leading to episodic resurfacing events and the formation of new crust (van Thienen et al., 2004). Not only did these processes cool the mantle, but also facilitated surface deformations, geochemical differentiation of the mantle and an increased rate of crustal evolution (Piccolo et al., 2019). Lithospheric dripping that involved mantle phase transitions and partial melting, particularly played an instrumental role in felsic melt generation from hydrated basalts, forming early stable continental masses in Earth's crustal evolution (Piccolo et al., 2019).

Recent studies have employed laboratory and numerical model simulations to investigate the growth behaviour of lithospheric drips. These model-based investigations show that drips grow typically with bulbous heads and narrow tails, much like Rayleigh–Taylor spikes (Piriz et al., 2023). Their necks become eventually thin, with the radius less than one fourth of that of their head (Andersen et al., 2024). The Rayleigh Taylor theory predicts a fastest-growing horizontal wavelength λ of gravitational instabilities on the order of a few lithospheric thicknesses, which decreases to $\sim$100–300 km for temperature-dependent viscosity and thermal diffusion properties (Conrad & Molnar, 1997). In case of periodic dripping, the lateral drip spacing equals roughly to λ, where individual drips have widths $\lesssim \lambda/2$

(McMillan & Schoenbohm, 2023). Drip instabilities grow exponentially with time in the linear regime, but subsequently begin to decelerate as their necks progressively narrow down (Conrad & Molnar, 1997). Experiments suggest that drips drastically reduce their descent rates at a vertical depth, proportionate to the lithospheric thickness when they develop a pronounced neck (radius ~¼ of the head) (Conrad & Molnar, 1997). Rheology and strain-rate feedbacks are crucial factors to strongly modulate their growth behaviour. A power-law viscous rheology (with $n \approx 3–4$) facilitates strain localization at the warmer base of the lithospheric lid, leading to preferential dripping in the weaker lower mantle lithosphere. In contrast, a Newtonian rheology or a lid with uniform temperature enables faster dripping (Göğüş & Pysklywec, 2008). The dripping behaviour can also significantly change due to other factors, such as imposed horizontal strain in the dripping layer. Slow compression tends to produce drips on large wavelengths ($\lambda \sim$ 4 to 6 times the lithospheric thickness), whereas extension/shear promotes the necking process during their descent (Conrad & Molnar, 1997).

Another major direction of drip research focuses on mineralogical phase transformations and eclogitization in mantle to identify the conditions in which gravitational instabilities give rise to lithospheric dripping, especially in the context of Archean tectonics. High-pressure MORB experiments suggest that eclogites can drastically increase their density due to the coesite-to-stishovite phase transition at approximately 9 GPa (Aoki & Takahashi, 2004). Such density hikes (by 10%–17%) facilitate the drip tectonics, resulting in removal of dense lithosphere (Austrheim, 1987; Doin & Henry, 2001; Jolivet et al., 2005) . It is now a well-established fact that phase transitions at various depths, such as the coesite-stishovite transition at ~200 km and the olivine-wadsleyite transition at ~500 km, determine the depth-dependent density of eclogitized MORB relative to the surrounding mantle, limiting the depth to which lithospheric drips can descend (Nishi et al., 2009). Although eclogites remain denser than peridotite in the entire upper mantle, their density difference progressively narrows down with increasing temperature and weakens the negative buoyancy required for dripping of lithospheric materials (Aoki & Takahashi, 2004). Based on numerical model results, Krystopowicz & Currie, 2013 have identified orogeny-driven crustal thickening as a critical factor in determining metamorphic eclogitization of the lowermost crust, fostering gravitational instabilities. Their interpretations suggest that density increase, even in modest levels (~7%) can support gravitationally driven removal processes. The presence of water is an additional factor in crustal weakening, which in turn facilitate the density-enhancing eclogitization process.

Despite the extensive research discussed above, a systematic parametric analysis is awaited to address the following key questions- what are the conditions in which lithospheric drips can penetrate into the lower mantle, how do they interact with mantle convection and plumes, and how do phase transitions govern the mode of dripping? These burning questions primarily constitute a motivational framework of the present study. Herein we adopt a thermo-chemical modelling approach to explore the varying modes of drip evolution through interactions with Earth's mantle. We investigate the transient nature of dripping through geological time, imposing conditions relevant to early Earth to establish its connection to the transition from stagnant to mobile lid tectonics (Figs. 1a,b). Our results bridge the various dripping mechanisms (superdrip formation, drip stagnation, and keel formation; Fig 1c) and their potential impacts on mantle convection pattern by examining the conditions for switchover from layered to whole mantle convection. Finally, we show qualitative and quantitative similarities between data obtained from our model and natural data, and discuss their implications for interpreting present-day lithospheric keels beneath thickened cratons.

2. Drip Modelling

We use the developer version of the finite element code ASPECT 2.4.0 (Bangerth et al., 2022a; Gassmöller et al., 2018; Heister et al., 2017; Kronbichler et al., 2012) to run our drip models in a 2D Cartesian space, covering the entire depth (~2890 km) of Earth's mantle and a horizontal distance of 8670 km. As this modelling primarily aims to study the dripping styles in the bulk lithosphere, we consider a 200 km thick lithosphere defined by a single compositional field (Table 1). The model lithosphere consists of two distinct layers: a basaltic crust and a pyrolitic mantle lithosphere (Fig. 2a). Phase changes are introduced at threshold depths of 40-120 km to initially implement eclogitization at the base of the thickened crust(Johnson et al., 2014), which is subsequently modified by further enhancement due to phase change in the mantle transition zone (Nishi et al., 2009). The sub-lithospheric mantle undergoes sequential phase transitions: olivine → wadsleyite at 410 km and ringwoodite → bridgmanite + periclase at 660 km (Table 1) (Bangerth et al., 2022a; Gassmöller et al., 2018; Heister et al., 2017; Kronbichler et al., 2012). Our thermo-chemical model simulations are run by treating the mantle as a stratified fluid region, with its density and viscosity varying as functions of pressure, temperature, chemical composition, and phase transformations (Fig. 2b).

2.1 Governing equations

Thermochemical convection simulations are implemented within a framework of the Boussinesq approximation, solving conservation equations for mass, momentum, and energy:

$$\nabla \cdot \boldsymbol{u} = 0, \tag{1}$$

$$\nabla P - \nabla \cdot [\mu \dot{\epsilon}] = \Delta \rho g e_z, \tag{2}$$

$$\rho_0 C_P \left(\frac{\partial T}{\partial t} + \boldsymbol{u} \cdot \nabla T \right) - \nabla \cdot K \nabla T = \rho_0 H, \tag{3}$$

where $\boldsymbol{u}$, P, μ, $\dot{\epsilon}$ denote velocity, dynamic pressure, viscosity, and strain rate, respectively. g is the gravitational acceleration, ρ_0 is the reference density of the ambient mantle, C_P is the specific heat at constant pressure, and T, K, and H are the absolute temperature, thermal conductivity, and the internal heating rate, respectively. To achieve Earth-like convective vigor, these parameters are chosen to fix the reference Rayleigh number:

$$Ra = \frac{\rho_0 g \alpha_0 \Delta T z^3}{\kappa_0 \mu_0}, \tag{4}$$

α_0, κ_0 and μ_0 represent the reference values of the coefficients of thermal expansion, the thermal diffusivity, and the viscosity of ambient mantle, respectively and ΔT is the temperature difference between the bottom (core-mantle boundary) and the top (surface) model boundaries. Most simulations are conducted keeping a reference Ra $\sim 5\times10^7$ (Table 1).

The Discontinuous-Galerkin method (He et al., 2017) is used to track compositional fields using the advection equation:

$$\frac{\partial \overline{c}}{\partial t} + (\boldsymbol{u}.\nabla \overline{c}) = 0, \tag{5}$$

where $\overline{c}$ denotes the compositional vector. The material properties are calculated from an incompressible base model that accounts for depth, temperature, and composition-dependent variations in density and viscosity. The depth-dependent viscosity is constrained by:

$$\mu(z, p, T, \overline{c}) = \frac{\mu(z)\mu_b(p, T, \overline{c})}{\mu_0}, \tag{6}$$

where ,

$$\mu_b(p, T, \overline{c}) = \mu_0 H_T exp\left(\frac{-A(T - T_0)}{T_0} \right) \zeta(\overline{c}), \tag{7}$$

A is the thermal viscosity exponent, T_0 the reference temperature, H_T a constant, and $\zeta(\overline{c})$ the compositional pre-factor (Bangerth et al., 2022a). μ_0 and μ_b represent reference viscosity and basal viscosity of the model, respectively. The material density is modelled as:

$$\rho\,(p,T,\overline{c}) = \big(1-\alpha(T-T_0)\big)\rho_0(z) + \Delta\rho_c c_0, \tag{8}$$

where $\Delta\rho_c$ is the compositional density contrast and c_0 is the first component of $\overline{c}$. The effects of phase transitions within the ambient mantle and the basal layer are incorporated by applying a phase function (Richter, 1973):

$$\Gamma = 0.5\left(1 + tanh\left(\frac{\Delta p}{\Delta p_0}\right)\right), \tag{9}$$

where Δp_0 is the pressure width of the transition zone and

$$\Delta p = p - p_{transition} - \gamma(T - T_{transition}), \tag{10}$$

where, γ represents the Clapeyron slope. We estimate dynamic topography from the model run, which is calculated from the radial stress component σ_{rr} at the surface (Liu & King, 2019) as:

$$h_{dt} = \frac{\sigma_{rr}}{(g.n)\rho'} \tag{11}$$

where ρ' is the density of the corresponding cell center, and $g.n$ is the vertical component of gravity.

2.2. Model boundary conditions and input parameters

To ensure realistic geodynamic behaviour, free-slip boundary conditions are applied to all four walls of the model box. In addition, isothermal boundary conditions are imposed at both the top and bottom surfaces of the model. The top and the bottom model boundaries that represent Earth's surface and the core-mantle boundary (CMB) are held at constant temperatures of 300 K and 4400 K (Hren et al., 2009; Nakagawa & Tackley, 2010), respectively. These fixed temperature conditions establish a thermal gradient that drives mantle convection in the model domain.

We introduce incipient geometrical perturbations at the base of the thickened basaltic crust (40-120 km) and basalt-eclogite phase transformation ($\Delta\rho_{CB}$) to initiate gravitational instability under a given initial density difference $\Delta\rho_P$ between the lithosphere and the underlying mantle region. An inherent relationship between the viscosities of the lithosphere and the ambient mantle is defined by a viscosity ratio M (Table 2). Also, the lithospheric drips

undergo significant density changes due to eclogite phase change in the mid-mantle within the transition zone (denoted by $\Delta\rho_{MM}$ hereafter) (Aoki & Takahashi, 2004; Nishi et al., 2009). Among these density changes, $\Delta\rho_{MM}$, is varied between 10 - 220 kg/m³ (Table 2) in the model simulation experiments, depending on the degrees of eclogitization (Krystopowicz & Currie, 2013). Similarly, considering the Archaean mantle conditions, we choose to vary $\Delta\rho_P$ and M accordingly (Table 2) in the model simulations. A parameter, termed buoyancy number B is used to incorporate the combined effect of initial density contrast and eclogitization, $\Delta\rho_P$ and $\Delta\rho_{CB}$. We obtained buoyancy number (B) for the lithosphere using the following formula-

$$B = \frac{\Delta\rho_{base}}{\rho*\alpha*\Delta T} = \frac{\Delta\rho_P + \Delta\rho_{CB}}{\rho*\alpha*\Delta T} \quad (12)$$

where $\Delta\rho_{base}$ is a sum of $\Delta\rho_P$ and $\Delta\rho_{CB}$, ρ is the reference density, α is the thermal expansion coefficient and ΔT is the temperature difference introduced between the top and bottom of the model domain, necessary for generating thermal convection. The range of B (0.03 to 0.79, Table 2) chosen in our simulations represent geodynamic settings with negatively buoyant, neutral and positively buoyant lithospheric with respect to the underlying mantle (Foley, 2018; Gerya, 2014).The present model setup introduces density changes in the dripping lithospheric and ambient mantle materials attributed to eclogitization of gabbro-rich dripping lithosphere (Austrheim, 1991; Austrheim et al., 1997; Bousquet et al., 1997) and mineralogical phase transitions in the peridotite-rich upper mantle Ganguly et al., 2009) respectively at specific depths.

3. Results

3.1 Dripping mechanisms

We ran a series of numerical simulations to assess the interactions of lithospheric drips with a convecting mantle, focusing particularly on the physical conditions (relatively thicker lithosphere and a higher potential temperature) applicable to the Archaean era (Capitanio et al., 2019; Gerya, 2014). These simulation runs allow us to recognize the following three principal mechanisms of drip evolution in the convecting mantle (Fig. 3).

Mechanism 1: Descending lithospheric drips cluster to form super-drip structures in upper mantle, which eventually penetrate through the 660 km phase transition zone and sink in

the lower mantle (Fig. 3b-i). This dripping mechanism modulates the whole-mantle convection pattern by creating strong downwelling zones.

Mechanism 2: Descending drips stagnate at the 660 km transition boundary, forming a distinct mechanical layer at the interface between the upper and lower mantle (Fig.3b-ii). The drip stagnation leads to partitioning of the mantle flow circulation into a layered convection structure.

Mechanism 3: Drips grow asymmetrically at the lithospheric base, developing inclined lithospheric keels in the form of proto-subduction structures (Fig. 3b-iii). This dripping mechanism leaves the lower mantle undisturbed, allowing the convective circulations to capture the whole mantle.

Each of these dripping mechanisms has specific geological consequences- both in the present scenario and those before the advent of plate tectonics. By examining their spatio-temporal characteristics, we identify major drip-driven processes in Earth's geodynamics.

3.1.1 Mechanism 1: Super-drip formation

Model simulation, run with parameters $B = 0.79$, $M = 10$ (Table 2) and , $\Delta\rho_{MM} = 200$ kg/m^{3}produced prominent lithospheric instabilities at ~ 20 Myr (Fig. 4a-i), which also lead to a sharp fall in heat flux and a steep rise in mean velocity values (Figs. 5a-i and b-i). These structures grew axi-symmetrically at high rates (~2.25×10^{-6}yr^{-1}) as negative Rayleigh-Taylor instabilities, with an average wavelength of 300 km. However, their initial growth was heterogeneous, with long-wavelength instabilities amplifying much faster (3×10^{-6} yr^{-1}) than short-wavelength instabilities (1.35×10^{-6}yr^{-1}) . The fast-growing instabilities eventually gave rise to large drips by capturing the materials from neighbouring slow-growing instabilities (Fig. 4a-ii). This inter-drip material transport is evident from relatively large horizontal flow velocity components ($v_x/v_z > 2$, Fig. 5c), which force smaller drips to deflect in their descent path towards the large drips (Fig. 4a-ii). Their clustering eventually forms a train of superdrip structures on a wavelength of ~ 2800 km (Fig. 4a-iii), separated by solitary vertical symmetrical drips. These drip clusters sink as single bodies, creating primary downwelling regions in the mantle. They show characteristically high sinking velocities (~ 3.9 cm/year), as compared to solitary drips that descend at much lower velocities (~2 cm/year, Fig. 5d). The superdrip structures continue dripping in Mechanism 1 to cross the 660 km barrier, and penetrate into the

lower mantle, keeping their material-supplying roots connected to the lithosphere. During this time the solitary drips remained halted in the mantle transition zone. They began to sink into the lower mantle following their detachment in the mid-mantle transition after a time lapse of 144 million years (Fig. 4a-iii).

Mechanism 1 dripping produces strong downwelling zones, coupled with equally intense upwelling zones (Fig. 4a-iv), setting in a whole-mantle convection (detailed discussion provided later in section 4.2). The drip clusters descend through the narrow (350-400 km) downwelling zones, forming sharp flow convergences in the velocity field. After crossing the 660 km boundary, they sink persistently at a high vertical velocity ($v_x/v_z < 1$, Fig. 5c), where the large axial drips pull the flanking smaller drips into the superdrip structures (Fig. 4a), ultimately to reach the core-mantle boundary. In contrast, minor solitary drips at the same time descend at much slower rates (Fig. 5d), remaining in the middle of the lower mantle, and they eventually fail to reach the CMB even after a computational run time of 188 Myr. During their interaction with the CMB the superdrips tend to symmetrically spread along the CMB at a velocity of ~0.7 cm/year on either side of their axis. This lateral movement eventually destabilizes the thermal boundary layer at the core-mantle boundary due to an increase of the local Rayleigh number to the critical Rayleigh number. This destabilization leads to initiation of thermal plumes originating from the CMB between two superdrip structures (Fig. 4a), also reflected by increases in heat flux values and mean velocity (Figs. 5a-i and b-i). The axial drips further interact with this newly formed plume. Some of the superdrips are reintroduced into upwelling process, mostly driven by the ascending mantle plumes. The whole-mantle convection drags part of superdrip materials upward to reach almost the base of the upper mantle (Fig. 4a-iv).

Following the drip event, the LAB attains significantly rough topography formed by asymmetric wavy irregularities on a wavelength of 400 km. In addition, the dripping process facilitates recycling of lithospheric materials, where the overall volume of the lithosphere reduces to ~65 % after the dominant phase of drip event, and further to ~ 50 % as the superdrips reach lower mantle (Fig. 5e). The rate of lithosphere removal varies with time. In the initial phase the rate is high (Fig. 5e), which drops drastically once the instabilities grows into mature drips that descend to lower mantle. Our model estimates suggest that the lithosphere becomes nearly half in its original thickness, i.e., nearly 100 km, as observed in the present-day oceanic plate-tectonic configurations.

3.1.2 Mechanism 2: Mid-mantle drip stagnation

Model simulation, run with the physical parameters: $B = 0.48$; $M = 10$ and $\Delta\rho_{MM}$ =100 kg/m^3 produce well-developed periodic (average wavelength: ~300 km) symmetrical drip structures at the lithospheric base at around 100 Myr (Fig. 4b-i,ii). The drop in heat flux rates with a synchronous rise in mean velocity is less effective in Mechanism 1 (Figs. 5a-ii and b-ii). Initially, the drip system evolves with strongly heterogeneous growth rates, where long-wavelength instabilities develop (growth rate: 1.68×10^{-6}yr^{-1}) much faster than short-wavelength ones (growth rate: 7.8×10^{-7}yr^{-1}). Over time, the rapidly growing instabilities dominate the dripping process by capturing lithospheric material from neighbouring, relatively slow-growing instabilities. This pull-driven horizontal flow ($v_x/v_z > 2$, Fig. 5c) becomes strong enough to deflect the descent paths of smaller drips, forcing them to converge and cluster around the faster-growing structures (Fig. 4b). These drip clusters form with an effective spacing (wavelength) of 2900 km (Fig. 4b), separated by vertically aligned, symmetrical solitary drips. Unlike the dripping behaviour observed in Mechanism 1, the drip clusters significantly reduce their descent rates, nearly coming to a halt (0.4-0.75 cm/year, Fig. 5d) near the mid-mantle transition zone, despite *B* being strongly positive . As a result, both the clustered and solitary drips become concentrated at approximately the same depth. In course of time individual drips progressively coalesce, flatten, and stagnate into a layer just beneath the 660 km phase transition boundary. This stagnated layer continues to accumulate smaller incoming drips (Fig. 4b), eventually reaching a finite thickness of ~150 km. This drip layer remains stable beneath the 660 km transition zone for a prolonged geological period (~170 Myr) until it is locally destabilized by thermal plumes, evident from the rise in heat flux and mean velocity(Figs. 5a-ii and b-ii). These plumes originate near the core–mantle boundary (CMB), ascend through the lower mantle, penetrate the 660 km transition, and then spread laterally within the upper mantle at ~200 km depth. The thermal perturbations introduced by the plumes destabilize the previously stagnant drip layer, selectively triggering its downward movement close to the plume head. As a consequence of dripping and plume action, the lithosphere erodes significantly but its initial rate is slower as compared to Mechanism 1 (Fig. 5e) These drips become neutrally buoyant in the lower mantle around ~1000 km depth and never reach the CMB (Fig. 4b-iv).

Drip stagnation at the 660 km transition results in partitioning in the mantle flow field, leading to generation of small-wavelength (300 km) convection cells in the upper mantle and large convective circulations in the lower mantle (as evident from v_x/v_z ratios, Fig. 5c). The overall pattern resembles typically a two-layer convection structure, unlike the whole-mantle convection observed in Mechanism 1, where the superdrip dynamics play a critical role in driving the convective circulations in the entire mantle. In case of Mechanism 2 dripping, the stagnated layer arrest the whole mantle convection, and split it into two-layer convection, where the upper mantle convection due to the additional effect of dripping is more vigorous ($Ra \sim 9\times10^7$) than the lower mantle ($Ra = 5\times10^7$), remaining unaffected by dripping. Relatively low $\Delta\rho_{MM}$ fails to empower the drips to cross the 660 km transition, and the stagnated drip layer thereby acts as a mechanical barrier to partition the mantle flows between the upper and lower mantle, leading to a layered convection, as suggested by Van Hunen & Moyen (2012).

3.1.3 Mechanism 3: Lithospheric keel-forming drips

Model condition set with B = 0.095, M = 10 and $\Delta\rho_{MM}$ = 100 kg/m^3 develop gravitational instabilities (Fig. 4c-i) at extremely slow rates (growth rate: 1.95×10^{-7}yr^{-1}) and they grow into drip-like structures (Fig.4c-ii) on a longer time scale (~240 Myr), as compared to those observed in Mechanisms 1 and 2. The drips do not show a typical axisymmetric shape with inverted bulbous geometry, rather they assume the shapes of narrow lithospheric keels. Their downward growth occurs at a slightly higher velocity (~0.158 cm/year). The lithospheric keels significantly differ from typical drip structures in their wavelengths (~300 and 650 km, respectively). Furthermore, during their downward growth they strongly interact with the thermal-plume heads undergoing lateral spreading beneath the lithosphere, as reflected from heat flux rates and mantle flow velocity ratios (Figs. 5a-iii and d). Such plume-keel interactions transform them into asymmetric orientations with inclinations in the range 40 to 50 degrees. The interactions also strongly influence the growth rates of keels, those closer to the plume head grow rapidly than those away from the plume and obliquely meet the mantle transition zone earlier at around ~300 Myr. The model eventually produces two regions of oppositely vergent keels, separated by a narrow zone of vertically symmetric keels (Fig. 4c-ii). The thermal plumes progressively begin to erode a large volume of lithospheric materials (Fig. 5e), and at the same time accelerate selectively the downward movement of the asymmetric keels, facilitating them to cross the 660 km barrier and penetrate into the lower mantle. However,

they fail to penetrate further into deeper levels due to their lower buoyancy, and occur as isolated small suspended bodies just beneath the transition zone.

Unlike the two mechanisms: 1 and 2, Mechanism 3 dripping influences the uppermost upper mantle dynamics, mediated mostly by horizontal flows of plume head, which is much higher than average convection velocity, as reflected in a sharp rise of v_x/v_z ratios (Fig. 5c). This suggests that the lower mantle convection has little control over the lithospheric dripping by Mechanism 3. Moreover, the effective lithospheric removal is much smaller (~3% of the initial volume after 500 Myr, Fig. 5e) than the corresponding removal amounts by Mechanisms 1 and 2. The removal rate also attains a peak when the plume head interacts with the keel structures (Fig. 4c-iii). To summarize, the keel structures undergo symmetric to asymmetric transformations under the horizontal convective flows in the upper mantle, forming subduction-like structures on a time scale of 350 Myr (Percival & Pysklywec, 2007). As time progresses, these structures evolve into proto-subduction-like formations at the base of upper mantle by 500 Myr (Fig.4c-iv), driven downward by the convective flow as they descend.

3.2 Drip evolution: Influence of geodynamic parameters

Each of Mechanism 1, 2, and 3 becomes active in a specific set of geodynamic condition, and undergoes a transition into the other mechanism with variations in the geodynamic parameters. In addition, our numerical simulations reveal subcritical geodynamic conditions that allow a lithosphere-mantle system to retain gravitational stability, leading no dripping to initiate even on an exceptionally long time scale (~1Gyr). In the following sub-sections, we show quantitatively parametric effects on the dripping behaviors, and finally present a synoptic field diagram of the three dripping mechanisms in a parametric space.

3.2.1 Control of initial lithospheric buoyancy

The buoyancy number B influences not only the dripping mechanisms, but also the convection style in Earth's mantle (detailed in section 4.2). $0.79 \geq B \geq 0.32$ enables Mechanism 1, with instabilities growing at rates of 9×10^{-7} - 2.25×10^{-6} yr^{-1}(Fig. 6a) leading to development of axisymmetric veritical drips with high dripping velocities(1.25 - 3.9 cm/year, Fig. 6a), ultimately forming super-drip structures in upper mantle, which eventually penetrate through the 660 km phase transition zone and sink in the lower mantle. Increasing B hardly influences

the drip behaviour described above, and maintains drip velocity magnitudes much higher than 1 cm/year(Fig. 6a). In contrast, $0.54 \geq B \geq 0.19$ results in a Mechanism 1 to Mechanism 2 transition, accompanied by a decrease in growth rate(3.63×10^{-7} - 1.75×10^{-6} yr^{-1}) and a drop of dripping velocity to values of 0.23 – 2.3 cm/year(Fig. 6a). Under such conditions, the evolving drips coalesce, flatten and stagnate at the 660 km phase transition boundary. This process, in turn, split the mantle flow field into small-scale convection cells in the upper mantle and a separate, longer wavelength convection in the lower mantle. Further decrease of B to values 0.03-0.16, leads to instabilities growing at very low growth rates(1.6×10^{-7} – 1.95×10^{-7} yr^{-1},Fig. 6a), transitioning from Mechanism 2 to Mechanism 3, forming mostly lithospheric keels at the LAB, with very low dripping velocities(0.05-0.4 cm/year, Fig. 6a), which strongly interact with dominantly horizontal convective flows in the upper mantle and develop persistently asymmetric geometry at 300 Myr (Percival & Pysklywec, 2007). This transition of dripping mechanism is also associated with a significant drop of heat flux (Fig. 6b) at the onset of dripping. $B \leq 0.03$ conditions do not produce any drips, leaving the mantle undisturbed and the flow completely driven by thermal convection.

3.2.2 Impact of the mid-mantle phase transitions

The density change ($\Delta\rho_{MM}$) in dripping materials at the mid-mantle transition zone is set as a function of varying proportions of their eclogitization and the P-T conditions in the upper mantle (Aoki & Takahashi, 2004; Nishi et al., 2009), whereas the density jumps for the ambient mantle, similar to the Archaean mantle (Ganguly et al., 2009) are kept constant. These density changes critically determine the dripping behaviour at the mid-mantle depth and their interactions with the convective flow in the mantle. The eclogite phase transition driven density change $\Delta\rho_{MM}$ at mantle transition zone critically control the dripping mechanisms. When $\Delta\rho_{base}$(section 2.2) > 75 kg/m^3, decreasing $\Delta\rho_{MM}$ below 150 kg/m^3 results in Mechanism 1 to 2 transition, leading to drip stagnation at the 660 km mantle transition. The heat flux values at dripping onset, also drops. At $\Delta\rho_{base}$ values of 70-75 kg/m^3, decreasing $\Delta\rho_{MM}$ below 200 kg/m^3 results in a transition to Mechanism 2 from Mechanism 1.When $\Delta\rho_{base}$ lies in the range of 60-70 kg/m^3, Mechanism 2 dripping occurs for the entire range of $\Delta\rho_{MM}$(10-220 kg/m^3). In the range 50-60 kg/m^3 of $\Delta\rho_{base}$, decreasing $\Delta\rho_{MM}$ below 200 kg/m^3 results in Mechanism 2 to 3 transition, as evident from the formation of asymmetric keels. Further, below values of 50 kg/m^3 of $\Delta\rho_{base}$, Mechanism 3 dripping for the entire range of $\Delta\rho_{MM}$(10-220 kg/m^3).

3.2.3 Influence of lithosphere/mantle viscosity ratio (*M*)

$M \approx 10$ conditions yield lithospheric dripping in both Mechanism 1 and 2 (Fig. 4a and b). Increasing M above 10 switches the transition of dripping mechanism into 3 (Fig. 4c). Increasing *M* reduces the growth rate of dripping at the lithospheric base while significantly reducing the heat flux at the onset of dripping. Large *M* ($\geq$20) conditions do not lead to any lithospheric drip formation.

3.2.4 Fields of drip mechanisms in a parametric space

Each of the three dripping mechanisms is activated in specific rheological configurations and physical conditions, such as model geometry, the depth-dependant phase-sensitive changes and the density perturbations chosen in our model simulations. Mechanism 1 dominates in lithospheric settings with viscosity ratios *M* in the order of 10 and Buoyancy number(section 2.2) $B \geq 0.29$; while eclogitization-driven density change in the mid-mantle $\Delta\rho_{MM} \geq 150$ kg/m^3 (Fig. 7). Drip clusters formed by this mechanism subsequently descend along downwelling zones, contributing to the whole-mantle convection (Fig. 4a, section 4.2). For the same B range, Mechanism 2 replaces Mechanism 1 when $\Delta\rho_{MM} < 150$ kg/m^3. (Fig. 7). This transition leads to a transformation of whole- to layered mantle convection (Fig. 4b, section 4.2). When B lies in the range 0.22-0.29, Mechanism 2 replaces Mechanism 1 when $\Delta\rho_{MM} <$ 200 kg/m^3. Between B values 0.19-0.22, Mechanism 2 dominates for entire range of $\Delta\rho_{MM}$ values(10 - 220 kg/m^3). For B values in the range 0.16-0.19, Mechanism 3 replaces Mechanism 2 when $\Delta\rho_{MM} <$ 200 kg/m^3. For higher viscosity ratios $M \geq 10$, $B < 0.16$, thereafter for entire range of $\Delta\rho_{MM}$ values(10 - 220 kg/m^3) a condition for Mechanism 3 dripping is set(Fig. 7), forming asymmetric lithospheric keel structures in the upper mantle dominated by horizontal convective flows (Fig. 4c, section 4.2).

4. Discussions

4.1 Drip mechanisms: Implications for Earth's geodynamic evolution

Gravitational dripping plays a major role in removal of basal materials from the lithosphere, recycling them back into the underlying mantle reservoir. Unlike delamination (rigid peeling away of lithospheric sheets along weak interfaces, (Beall et al., 2017; Chowdhury

et al., 2017), the dripping is typically an axisymmetric sinking process, initiated by Rayleigh-Taylor instabilities in a viscous flow regime. Our model results suggest that the initial lithospheric buoyancy, phase transitions (including eclogitization) at the mid-mantle transition zone, and viscosity contrasts between lithosphere and the underlying mantle primarily determine the modes of dripping, categorized as Mechanism 1, 2, and 3 in this study. Each of these mechanisms results in distinctive impacts on the mantle geodynamics. For instance, super-drip structures produced in Mechanism 1 concentrate preferentially in the downwelling zones, sink across the mantle phase transition boundaries, and eventually accumulate above the core-mantle boundary (CMB) (Fig. 4a). This process facilitates destabilization of the thermal boundary layer at the CMB, triggering the initiation of thermal plumes in the convergent zones between two laterally spreading super-drip structures. The super-drip structures are analogous to LLSVPs, which represent long-term accumulations of dense, subducted oceanic crust and sediments in the lowermost mantle (Christensen & Hofmann, 1994; Niu, 2018; Panton et al., 2023, 2025). Geochemical and isotopic analyses, such as Sr–Nd–Pb systematics, heavy δ^{65} Cu signatures, and Fe-isotope variations in ocean-island basalts, provide direct evidence that recycled crustal materials are entrained into these upwellings (Soderman et al., 2023; Yao et al., 2025), similar to that observed in Mechanism 1 dripping. These geological fingerprints indicate that during the Hadean Era the Earth experienced geodynamic evolution dominated by lithospheric superdrips that strongly modulated the mantle convection pattern and generation of abundant thermal plumes, originating predominantly in the lower mantle. Furthermore, Mechanism 1 dripping was largely responsible for a whole-mantle convection, characterized by high advection velocity (Fig. 6c), sharper drops in heat flux (Figs. 5a & 6b) and higher rates of LAB erosion (Fig. 5e), which are all well documented from geological records. Drips produced in Mechanism 2, in contrast, stagnate at the 660 km boundary, forming a distinct mechanical layer that partitions the convective flows into upper and lower mantle. This mechanism consequently leaves the lower mantle mostly unaffected by drip activities- a geodynamic condition that represents the early to mid-Archean scenario of lithospheric characteristics. The lithosphere by this time became more positively buoyant due to more differentiated felsic material accretion(Drabon et al., 2024; Tang et al., 2024). Based on the available estimates, the buoyancy B is expected to decrease by ~ 0.2, triggering Mechanism 2 in the system (Fig. 6a). The drip stagnation at 660 km, which locally divided the whole mantle convection into two: a more vigorous upper mantle convection, dominated by horizontal flows ($v_x/v_z > 1$, Fig. 6c-iii, $Ra \sim 9\times10^7$), and a much calmer lower mantle convection ($Ra \sim 5\times10^7$). The end phase of Archean produced thermal plumes in the lower mantle, which ascended to

upper mantle and destabilized the stagnated drips, locally disrupting the two-layer convection structure. Increased plume activity subsequently impacted the mantle dynamics during late Archaean. The laterally spreading plume heads advectively erodes the LAB, forming asymmetric lithospheric keels, instead of typical axisymmetric drips , which resembles proto-subduction zones, as observed in Mechanism 3 model (Fig. 4c). These transformations in dripping mechanisms eventually led to the onset of modern plate tectonics (Beall et al., 2017; Foley, 2018; Stern, 2018) through reactivation of earlier drip-induced proto-subduction structures in lithosphere.

To sum up, Earth's tectonic evolution, especially during Hadean Era occurred in relatively hotter mantle condition, dominated by Mechanism 1 dripping and whole-mantle convective circulations (Fig. 1b). With time, the mantle cooled down, and the vigorousity of Earth's mantle convection reduced, leading to Mechanism 2 dripping in early to mid-Archean. This trend continued through to late Archaean and attained a mantle condition that favoured Mechanism 3 dripping, forming asymmetric lithospheric keels that acted as precursors for the initiation of modern-day plate tectonics.

4.2 Controls of dripping on mantle convection

The negative buoyancy of individual drips in superdrip structures (Mechanism 1) cumulatively becomes strong enough to create large-scale downwelling zones at a wavelength of ~2800 km, which interact with the CMB and destabilize the thermal boundary layer (TBL). The superdrip - TBL interactions eventually gives to regular upwelling zones. These concomitantly operating downwelling and upwelling flows give rise to a vigorous whole-mantle convection on a wavelength of ~2800 km. At this stage the super-drip dynamics completely captures the thermal convection with an overall Rayleigh number in the order of 10^7. Several studies have shown that Earth's Early Archean geodynamics was dominated by layered mantle convection due to higher *Ra* and enhanced thermal states in the mantle (Van Hunen & Moyen, 2012). However, recent model investigations suggest that excess mantle temperatures can facilitate the 660 km mineralogical phase transition due its negative Clapeyron slope, which in turn favours sinking of lithospheric slabs into the lower mantle under their negative buoyancy (Ganguly et al., 2009). Such a recycling mechanism might contribute to whole-mantle convection generation in the Hadean geodynamic system (Fig. 1b). On the other hand, many geoscientists strongly claim lithospheric dripping as a dominant recycling process in the Earth's tectonic evolution(Beall et al., 2017; Johnson et al., 2014; Stern,

2018).The present study suggests that the dripping process in Mechanism 1 could be an additional factor to promote the whole-mantle convection in Earth's early tectonics.

The switching dripping mechanisms also played a critical role in regulating the transient behaviour of mantle convection, especially in the early Archean geodynamics. The drip stagnation, produced by Mechanism 2 at the 660 km transition zone results in partitioning of the mantle convection into two regimes: vigorous convection in the upper mantle (Ra~9×10^7) and relatively weaker convection (Ra ~5×10^7) (Fig. 8a). The pattern broadly resembles a stratified mantle convection structure: a vigorously convecting, isotopically depleted upper mantle overlying a relatively quiescent, compositionally distinct lower mantle, in the Archean time (Van Hunen & Moyen, 2012). Various lines of studies- numerical simulations, laboratory analogs, and xenon-Ti isotope data indicate that thermal plumes originated in lower mantle rarely penetrated the ~660 km boundary and that upper–lower mantle had little material exchange(Ballmer et al., 2015; Ogawa, 2018; van Keken et al., 2002). During this phase, the drip stagnation at mid-mantle depths could be a major factor to impede the deep mixing between the upper and the lower mantle until the geodynamic setting underwent a major transition into whole-mantle plate tectonics in a later phase of Earth's history(Bercovici & Karato, 2003).

Earth's geodynamics underwent again a remarkable transition during the late Archaean time, leading to development of whole-mantle convection and plume activities on long wavelengths. The present model results suggest that the lower mantle convection hardly experienced any impacts of the lithospheric dripping process, unlike those observed during Hadean time. In addition, effective lithospheric removal by dripping becomes significantly weak, leaving the major part of mantle dominated by thermally-driven convection (Fig. 8).

4.3 Phanerozoic tectonics: impact of lithospheric drip activities

Geophysical evidences, e.g., gravity anomalies, seismic tomography, and Moho depth variations suggest that lithospheric dripping is still an active process in in the modern-day Phanerozoic belts across the globe (McMillan & Schoenbohm, 2023). For example, collisional plate-tectonic settings, like the Himalayan–Tibetan orogen, provides a spectacular framework of lithospheric dripping. Such dripping occurs due to intense crustal thickening and onset of Rayleigh–Taylor instabilities, leading to detachment of dense mantle root (England & Houseman, 1989). This instability is delayed until substantial thickening occurred, and the

process afterward evolved on much shorter time scales, as compared to the overall collision timescale, switching a kinematic transition from convergence to extension. England and Houseman (1989) used viscous-convection models to show partial delamination of the lower lithosphere as an underlying mechanism for several Tibetan Plateau phenomena (Houseman & Molnar, 1997). Their models, quite akin to the dripping mechanism 3 (Figs. 3b-iii & 4c), also predict that removal of the refractory root injects heat into the plateau, resulting in thermally weakening that led to kilometre-scale surface uplift in response to the asthenospheric flows beneath Tibet (Houseman et al., 2025). This model interpretation finds observational support in Tibet, such as anomalously thin or absence of mantle lithosphere beneath the plateau, widespread ultrapotassic volcanism and low-velocity zones marking drip events (Chen et al., 2017; Song & Klemperer, 2024). Moreover, their model resolves the paradox of high mantle velocities coexisting with late-stage extension and volcanism, taking into account removal of deep dense root by dripping, leaving a shallow high-velocity keel and accumulation of heat and volatiles that in turn gave rise to potassic magmatism in the crust (Houseman et al., 2025). Lithospheric dripping thus emerges as an active tectonic mechanism that plays crucial role in plateau uplift, transient magmatism, crustal weakening and eventual extensional collapse in continental orogens (England & Houseman, 1989; Houseman et al., 2025).

In SE Carpathians (Romania), the gravity anomalies are interpreted to represent regions of gravitational instabilities in the lithosphere, suggesting that dense lithospheric materials are dripping into the asthenosphere. Quite similar to mechanism 3 (Fig. 3b-iii), the high velocity anomaly driven by RT instability is flanked by low-velocity upwelling zones formed due to the ambient mantle convective flow. This process (Fig. 9-ii) eventually drives intra-orogenic extension and basin formation, e.g., the rapid Miocene opening of the Pannonian Basin concurrently with the Carpathian orogeny (Ren et al., 2012). This dripping naturally accounts for a range of observables, such as differential extension between crust and mantle, arcuate geometry of the mountain belt and deep (~200 km) seismicity beneath the Vrancea region in the SE Carpathians (Houseman & Gemmer, 2007). Similarly, beneath the Central Anatolian Plateau in Turkey, pronounced negative gravity anomalies align with mantle flow patterns, which suggest the possibility of substantial lithospheric removal (Göğüş et al., 2017). Seismic imaging reveals vertically elongated high-velocity anomalies in the upper mantle that indicate detached lithospheric fragments in the mantle (Fig. 9-iv), which resemble drips produced by mechanism 3 dripping. In South America, similar negative anomalies occur beneath the Southern Puna and the Central Arrizaro regions in Argentina (Calixto et al., 2013), and beneath

588 the Hindu Kush in Asia (Koulakov, 2011). These geophysical observations attest the occurrence
589 of lithospheric dripping in continental settings (Fig.9-i, v). The Isabella Anomaly (California,
590 USA), located beneath the southern Great Valley and southwestern Sierra Nevada, features a
591 high-density structure extending from 100 to 200 km depth (Cox et al., 2016). Gravity
592 modelling portrays this anomaly as a rectangular lithospheric root dipping north-eastward at
593 approximately 65°. Seismic tomography reveals a high-velocity anomaly (V_p ~ 4.6–4.7 km/s)
594 supporting the presence of an actively sinking drip (Fig. 9-vi). Variations in Moho depth, from
595 ~23 km in the Great Valley to over 40 km beneath the Sierra Nevada, indicate crustal thinning
596 associated with lithospheric removal. In most of such observed seismic high-velocity anomaly
597 zones (Fig. 9), the principal mechanism driving lithospheric dripping is analogous to
598 mechanism 3, involving mantle flow upwelling or plume assisted dripping.

599

600 **5. Summary and Outlook**
601

602 Using thermo-chemical models we investigated the phenomenon- lithospheric dripping during
603 overall tectono-thermal evolution of the Earth through geological time. This investigation
604 identifies three distinct mechanisms of dripping- *Mechanism 1*: clustering of lithospheric drips
605 to form superdrips that penetrate across the 660 km mid-mantle transition zone and sink as
606 single bodies in the lower mantle; *Mechanism 2*: stagnation of individual drips, forming a
607 mechanical layer at the 660 km barrier; and *Mechanism 3*: strongly asymmetric dripping,
608 forming keels at the lithospheric base. Each of these mechanisms distinctively modulate
609 thermal convection patterns in the mantle. The super-drip driven downwelling in Mechanism
610 1 captures the convection dynamics, leading to development of whole-mantle convection on
611 an average wavelength of ~2800 km. In contrast, Mechanism 2 gives rise to a layered
612 convection due to flow partitioning by the drip stagnation at the 660 km boundary. Mechanism
613 3, on the other hand, allows the thermal convection to occur in the whole mantle on larger
614 wavelengths ~4200 km. Our study also finds a connection between lithospheric dripping and
615 plume generation at the thermal boundary layer (TBL) above the core-mantle boundary.
616 Mechanism 1 facilitates the destabilization of the TBL, aided by drip interactions, which in
617 turn increases the spatial frequency of plume formation in the mantle. Additionally, our drip
618 models account for diverse geophysical fingerprints (seismic tomography, gravity anomalies,

Moho geometry) observed in thickened cratonic regions like the Rio Grande Rift, SE Carpathians, and the Isabella anomaly.

Based on our drip model findings, we present a projected outlook on the debated scenarios of Earth's early geodynamic evolution (Fig. 10). During Hadean times, eclogitization might be more active to promote the process of lithospheric dripping in Mechanism 1. The resulting drips evolved through self-organization into mechanically coherent clusters (large super-drips) that modulated whole-mantle convective circulation, and rapid lithospheric erosion. The overall vertical lithospheric tectonics was controlled by the combined actions of superdrip-driven downwelling and plume upwelling in mantle. With progressive mantle cooling, Mechanism 2 became active, and transformed the whole-mantle convection into two-layer convection and chemical stratification, which might represent the early Archean geodynamic setting. Further cooling and rheological evolution led to a stage of proto-subduction keel formation by Mechanism 3 in the uppermost mantle. These transitions of dripping mechanism provided a key mechanical pathway linking vertical foundering in a pre-plate-tectonic (stagnant/sluggish-lid) regime to the emergence of plate tectonics by generating keels that subsequently evolved into plate boundaries.

Acknowledgement

The present work has been supported by the UGC through the Senior Research Fellowship to SB, an INSPIRE faculty fellowship (DST/INSPIRE/04/2022/002647) granted by Department of Science and Technology (DST), India to DG and by DST-SERB through the J. C. Bose fellowship (JBR/2022/000003) to NM. The Computational Infrastructure for Geodynamics (geodynamics.org), funded by the National Science Foundation under awards EAR-0949446 and EAR-1550901 is acknowledged for supporting the development of ASPECT.

References

Andersen, A. J., Göğüş, O. H., Pysklywec, R. N., Şengül Uluocak, E., & Santimano, T. (2024). Multistage lithospheric drips control active basin formation within an uplifting orogenic plateau. *Nature Communications 2024 15:1*, *15*(1), 1–10. https://doi.org/10.1038/s41467-024-52126-7

Aoki, I., & Takahashi, E. (2004). Density of MORB eclogite in the upper mantle. *Physics of the Earth and Planetary Interiors*, *143–144*(1–2), 129–143. https://doi.org/10.1016/J.PEPI.2003.10.007

Austrheim, H. (1987). Eclogitization of lower crustal granulites by fluid migration through shear zones. *Earth and Planetary Science Letters*, *81*(2–3), 221–232. https://doi.org/10.1016/0012-821X(87)90158-0

Austrheim, H. (1991). Eclogite formation and dynamics of crustal roots under continental collision zones. *Terra Nova*, *3*(5), 492–499. https://doi.org/10.1111/j.1365-3121.1991.tb00184.x

Austrheim, H., Erambert, M., & Engvik, A. K. (1997). Processing of crust in the root of the Caledonian continental collision zone: the role of eclogitization. *Tectonophysics*, *273*(1–2), 129–153. https://doi.org/10.1016/S0040-1951(96)00291-0

Ballmer, M. D., Schmerr, N. C., Nakagawa, T., & Ritsema, J. (2015). Compositional mantle layering revealed by slab stagnation at ~1000-km depth. *Science Advances*, *1*(11). https://doi.org/10.1126/SCIADV.1500815

Bangerth, W., Dannberg, J., Fraters, M., Gassmoeller, R., Glerum, A., Heister, T., Myhill, R., & Naliboff, J. (2022). *ASPECT v2.4.0*. https://doi.org/10.5281/ZENODO.6903424

Beall, A. P., Moresi, L., & Stern, T. (2017). Dripping or delamination? A range of mechanisms for removing the lower crust or lithosphere. *Geophysical Journal International*, *210*(2), 671–692. https://doi.org/10.1093/GJI/GGX202

Bercovici, D., & Girard, J. (2025). A two-and-a-half-dimensional flexing-drip model of lithospheric instabilities and proto-subduction (with two-phase grain-damage). *Physics of the Earth and Planetary Interiors*, *367*, 107403. https://doi.org/10.1016/J.PEPI.2025.107403

Bercovici, D., & Karato, S. I. (2003). Whole-mantle convection and the transition-zone water filter. *Nature*, *425*(6953), 39–44. https://doi.org/10.1038/NATURE01918

Bousquet, R., Goffé, B., Henry, P., Le Pichon, X., & Chopin, C. (1997). Kinematic, thermal and petrological model of the Central Alps: Lepontine metamorphism in the upper crust and eclogitisation of the lower crust. *Tectonophysics*, *273*(1–2), 105–127. https://doi.org/10.1016/S0040-1951(96)00290-9

Calixto, F. J., Sandvol, E., Kay, S., Mulcahy, P., Heit, B., Yuan, X., Coira, B., Comte, D., & Alvarado, P. (2013). Velocity structure beneath the southern Puna plateau: Evidence for delamination. *Geochemistry, Geophysics, Geosystems*, *14*(10), 4292–4305. https://doi.org/10.1002/ggge.20266

Capitanio, F. A., Nebel, O., Cawood, P. A., Weinberg, R. F., & Chowdhury, P. (2019). Reconciling thermal regimes and tectonics of the early Earth. *Geology*, *47*(10), 923–927. https://doi.org/10.1130/G46239.1

Chen, M., Niu, F., Tromp, J., Lenardic, A., Lee, C. T. A., Cao, W., & Ribeiro, J. (2017). Lithospheric foundering and underthrusting imaged beneath Tibet. *Nature Communications*, *8*(1), 1–10. https://doi.org/10.1038/NCOMMS15659

Chowdhury, P., Gerya, T., & Chakraborty, S. (2017). Emergence of silicic continents as the lower crust peels off on a hot plate-tectonic Earth. *Nature Geoscience*, *10*(9), 698–703. https://doi.org/10.1038/NGEO3010

Christensen, U. R., & Hofmann, A. W. (1994). Segregation of subducted oceanic crust in the convecting mantle. *Journal of Geophysical Research: Solid Earth*, *99*(B10), 19867–19884. https://doi.org/10.1029/93JB03403

Conrad, C. P., & Molnar, P. (1997). The growth of Rayleigh—Taylor-type instabilities in the lithosphere for various rheological and density structures. *Geophysical Journal International*, *129*(1), 95–112. https://doi.org/10.1111/J.1365-246X.1997.TB00939.X

Cox, P., Stubailo, I., & Davis, P. (2016). Receiver Function and Geometric Tomography along the Monterey Microplate to Test Slab Delamination or Lithospheric Drip Models of the Isabella Anomaly, California. *Bulletin of the Seismological Society of America*, *106*(1), 267–280. https://doi.org/10.1785/0120140339

Doin, M. P., & Henry, P. (2001). Subduction initiation and continental crust recycling: the roles of rheology and eclogitization. *Tectonophysics*, *342*(1–2), 163–191. https://doi.org/10.1016/S0040-1951(01)00161-5

Drabon, N., Kirkpatrick, H. M., Byerly, G. R., & Wooden, J. L. (2024). Trace elements in zircon record changing magmatic processes and the multi-stage build-up of Archean proto-continental crust. *Geochimica et Cosmochimica Acta*, *373*, 136–150. https://doi.org/10.1016/J.GCA.2024.03.014

England, P., & Houseman, G. (1989). Extension during continental convergence, with application to the Tibetan Plateau. *Journal of Geophysical Research: Solid Earth*, *94*(B12), 17561–17579. https://doi.org/10.1029/JB094IB12P17561

Foley, B. J. (2018). The dependence of planetary tectonics on mantle thermal state: Applications to early Earth evolution. *Philosophical Transactions of the Royal Society A: Mathematical, Physical and Engineering Sciences*, *376*(2132). https://doi.org/10.1098/RSTA.2017.0409

Ganguly, J., Freed, A. M., & Saxena, S. K. (2009). Density profiles of oceanic slabs and surrounding mantle: Integrated thermodynamic and thermal modeling, and implications for the fate of slabs at the 660 km discontinuity. *Physics of the Earth and Planetary Interiors*, *172*(3–4), 257–267. https://doi.org/10.1016/J.PEPI.2008.10.005

Gassmöller, R., Lokavarapu, H., Heien, E., Puckett, E. G., & Bangerth, W. (2018). Flexible and Scalable Particle-in-Cell Methods With Adaptive Mesh Refinement for Geodynamic Computations. *Geochemistry, Geophysics, Geosystems*, *19*(9), 3596–3604. https://doi.org/10.1029/2018GC007508

Gerya, T. (2014). Precambrian geodynamics: Concepts and models. *Gondwana Research*, *25*(2), 442–463. https://doi.org/10.1016/J.GR.2012.11.008

Gerya, T. (2019). Geodynamics of the early Earth: Quest for the missing paradigm. *Geology*, *47*(10), 1006–1007. https://doi.org/10.1130/FOCUS102019.1

Göğüş, O. H., & Pysklywec, R. N. (2008). Near-surface diagnostics of dripping or delaminating lithosphere. *Journal of Geophysical Research: Solid Earth*, *113*(B11), 11404. https://doi.org/10.1029/2007JB005123

Göğüş, O. H., Pysklywec, R. N., Şengör, A. M. C., & Gün, E. (2017). Drip tectonics and the enigmatic uplift of the Central Anatolian Plateau. *Nature Communications*, *8*(1), 1–9. https://doi.org/10.1038/S41467-017-01611-3

He, Y., Puckett, E. G., & Billen, M. I. (2017). A discontinuous Galerkin method with a bound preserving limiter for the advection of non-diffusive fields in solid Earth geodynamics. *Physics of the Earth and Planetary Interiors*, *263*, 23–37. https://doi.org/10.1016/J.PEPI.2016.12.001

Heister, T., Dannberg, J., Gassmöller, R., & Bangerth, W. (2017). High accuracy mantle convection simulation through modern numerical methods – II: realistic models and problems. *Geophysical Journal International*, *210*(2), 833–851. https://doi.org/10.1093/GJI/GGX195

Houseman, G. A., England, P. C., & Evans, L. A. (2025). Gravitational instability of thickened yet compositionally buoyant Tibetan mantle lithosphere. *Tectonophysics*, *911*, 230837. https://doi.org/10.1016/j.tecto.2025.230837

Houseman, G. A., & Gemmer, L. (2007). Intra-orogenic extension driven by gravitational instability: Carpathian-Pannonian orogeny. *Geology*, *35*(12), 1135–1138. https://doi.org/10.1130/G23993A.1

Houseman, G. A., & Molnar, P. (1997). Gravitational (Rayleigh-Taylor) instability of a layer with non-linear viscosity and convective thinning of continental lithosphere. *Geophysical Journal International*, *128*(1), 125–150. https://doi.org/10.1111/J.1365-246X.1997.TB04075.X

Hren, M. T., Tice, M. M., & Chamberlain, C. P. (2009). Oxygen and hydrogen isotope evidence for a temperate climate 3.42 billion years ago. *Nature*, *462*(7270), 205–208. https://doi.org/10.1038/NATURE08518

Johnson, T. E., Brown, M., Kaus, B. J. P., & Vantongeren, J. A. (2014). Delamination and recycling of archaean crust caused by gravitational instabilities. *Nature Geoscience*, *7*(1), 47–52. https://doi.org/10.1038/NGEO2019

Jolivet, L., Raimbourg, H., Labrousse, L., Avigad, D., Leroy, Y., Austrheim, H., & Andersen, T. B. (2005). Softening trigerred by eclogitization, the first step toward exhumation during continental subduction. *Earth and Planetary Science Letters*, *237*(3–4), 532–547. https://doi.org/10.1016/J.EPSL.2005.06.047

Koulakov, I. (2011). High-frequency P and S velocity anomalies in the upper mantle beneath Asia from inversion of worldwide traveltime data. *Journal of Geophysical Research: Solid Earth*, *116*(4), 4301. https://doi.org/10.1029/2010JB007938

Kronbichler, M., Heister, T., & Bangerth, W. (2012). High accuracy mantle convection simulation through modern numerical methods. *Geophysical Journal International*, *191*(1), 12–29. https://doi.org/10.1111/J.1365-246X.2012.05609.X

Krystopowicz, N. J., & Currie, C. A. (2013). Crustal eclogitization and lithosphere delamination in orogens. *Earth and Planetary Science Letters*, *361*, 195–207. https://doi.org/10.1016/J.EPSL.2012.09.056

Lei, T., Li, Z. H., & Liu, M. (2019). Removing mantle lithosphere under orogens: delamination versus convective thinning. *Geophysical Journal International*, *219*(2), 877–896. https://doi.org/10.1093/GJI/GGZ329

Lev, E., & Hager, B. H. (2008). Rayleigh–Taylor instabilities with anisotropic lithospheric viscosity. *Geophysical Journal International*, *173*(3), 806–814. https://doi.org/10.1111/J.1365-246X.2008.03731.X

Levander, A., Schmandt, B., Miller, M. S., Liu, K., Karlstrom, K. E., Crow, R. S., Lee, C. T. A., & Humphreys, E. D. (2011). Continuing Colorado Plateau uplift by delamination-style convective lithospheric downwelling. *Nature*, *472*(7344), 461–465. https://doi.org/10.1038/NATURE10001

Liu, S., & King, S. D. (2019). A benchmark study of incompressible Stokes flow in a 3-D spherical shell using ASPECT. *Geophysical Journal International*, *217*(1), 650–667. https://doi.org/10.1093/GJI/GGZ036

Long, M. D., Wagner, L. S., King, S. D., Evans, R. L., Mazza, S. E., Byrnes, J. S., Johnson, E. A., Kirby, E., Bezada, M. J., Gazel, E., Miller, S. R., Aragon, J. C., & Liu, S. (2021). Evaluating Models for Lithospheric Loss and Intraplate Volcanism Beneath the Central Appalachian Mountains. *Journal of Geophysical Research: Solid Earth*, *126*(10), e2021JB022571. https://doi.org/10.1029/2021JB022571

McMillan, M., & Schoenbohm, L. M. (2023). Diverse Styles of Lithospheric Dripping: Synthesizing Gravitational Instability Models, Continental Tectonics, and Geologic Observations. *Geochemistry, Geophysics, Geosystems*, *24*(2), e2022GC010488. https://doi.org/10.1029/2022GC010488

Nakagawa, T., & Tackley, P. J. (2010). Influence of initial CMB temperature and other parameters on the thermal evolution of Earth's core resulting from thermochemical spherical mantle convection. *Geochemistry, Geophysics, Geosystems*, *11*(6), 6001. https://doi.org/10.1029/2010GC003031

Nishi, M., Kubo, T., Kato, T., Nishi, M., Kubo, T., & Kato, T. (2009). Metastable transformations of eclogite to garnetite in subducting oceanic crust. *Journal of Mineralogical and Petrological Sciences*, *104*(3), 192–198. https://doi.org/10.2465/JMPS.080929

Niu, Y. (2018). Origin of the LLSVPs at the base of the mantle is a consequence of plate tectonics – A petrological and geochemical perspective. *Geoscience Frontiers*, *9*(5), 1265–1278. https://doi.org/10.1016/J.GSF.2018.03.005

Ogawa, M. (2018). Magmatic differentiation and convective stirring of the mantle in early planets: the effects of the magmatism-mantle upwelling feedback. *Geophysical Journal International*, *215*(3), 2144–2155. https://doi.org/10.1093/GJI/GGY413

Panton, J., Davies, J. H., Koelemeijer, P., Myhill, R., & Ritsema, J. (2025). Unique composition and evolutionary histories of large low velocity provinces. *Scientific Reports*, *15*(1), 4466. https://doi.org/10.1038/s41598-025-88931-3

Panton, J., Davies, J. H., & Myhill, R. (2023). The Stability of Dense Oceanic Crust Near the Core-Mantle Boundary. *Journal of Geophysical Research: Solid Earth*, *128*(2), e2022JB025610. https://doi.org/10.1029/2022JB025610

Percival, J. A., & Pysklywec, R. N. (2007). Are Archean lithospheric keels inverted? *Earth and Planetary Science Letters*, *254*(3–4), 393–403. https://doi.org/10.1016/J.EPSL.2006.11.047

Piccolo, A., Palin, R. M., Kaus, B. J. P., & White, R. W. (2019). Generation of Earth's Early Continents From a Relatively Cool Archean Mantle. *Geochemistry, Geophysics, Geosystems*, *20*(4), 1679–1697. https://doi.org/10.1029/2018GC008079

Piriz, A. R., Piriz, S. A., & Tahir, N. A. (2023). Formation of spikes and bubbles in the linear phase of Rayleigh-Taylor instability in elastic-plastic media. *Physical Review E*, *107*(3), 035105. https://doi.org/10.1103/PHYSREVE.107.035105

Ren, Y., Stuart, G. W., Houseman, G. A., Dando, B., Ionescu, C., Hegedüs, E., Radovanović, S., & Shen, Y. (2012). Upper mantle structures beneath the Carpathian–Pannonian region: Implications for the geodynamics of continental collision. *Earth and Planetary Science Letters*, *349–350*, 139–152. https://doi.org/10.1016/J.EPSL.2012.06.037

Richter, F. M. (1973). Convection and the large-scale circulation of the mantle. *Journal of Geophysical Research*, *78*(35), 8735–8745. https://doi.org/10.1029/JB078I035P08735

Soderman, C. R., Shorttle, O., Gazel, E., Geist, D. J., Matthews, S., & Williams, H. M. (2023). The evolution of the Galápagos mantle plume. *Science Advances*, *9*(10). https://doi.org/10.1126/SCIADV.ADD5030

Song, X., & Klemperer, S. (2024). *Himalayan sub-Moho earthquakes suggest crustal faults trigger eclogitized-drip tectonics*. https://doi.org/10.21203/RS.3.RS-5051130/V1

Stern, R. J. (2018). The evolution of plate tectonics. *Philosophical Transactions of the Royal Society A: Mathematical, Physical and Engineering Sciences*, *376*(2132). https://doi.org/10.1098/RSTA.2017

Tang, M., Chen, H., Song, S., Sun, G., & Wang, C. (2024). Zircon Eu/Eu* in Archean TTGs with implications for the role of endogenic oxidation in Archean crustal differentiation. *Geochimica et Cosmochimica Acta*, *378*, 259–269. https://doi.org/10.1016/J.GCA.2024.06.031

Van Hunen, J., & Moyen, J. F. (2012). Archean subduction: Fact or fiction? *Annual Review of Earth and Planetary Sciences*, *40*(Volume 40, 2012), 195–219. https://doi.org/10.1146/ANNUREV-EARTH-042711-105255

van Keken, P. E., Hauri, E. H., & Ballentine, C. J. (2002). Mantle mixing: The generation, preservation and destruction of chemical heterogeneity. *Annual Review of Earth and Planetary Sciences*, *30*(Volume 30, 2002), 493–525. https://doi.org/10.1146/ANNUREV.EARTH.30.091201.141236

van Thienen, P., van den Berg, A. P., & Vlaar, N. J. (2004). Production and recycling of oceanic crust in the early Earth. *Tectonophysics*, *386*(1–2), 41–65. https://doi.org/10.1016/J.TECTO.2004.04.027

Yao, J., Yuan, W., Wang, Z., Moynier, F., Zhu, W. G., Wu, Y. D., An, Y., & Chen, J. (2025). Copper isotope evidence for recycled crustal sulfides in deep mantle plume source. *Communications Earth and Environment*, *6*(1), 1–11. https://doi.org/10.1038/S43247-025-02468-X

Figure Captions

Figure 1. a) Evolution of major tectonic regimes in Earth's history. The graphical plots show corresponding variations in potential temperature, crustal reworking and $\delta^{18}O$ values through geologic time. The shaded region indicates abundance of eclogite (modified after McMillan & Schoenbohm, 2023). b) Global tectonic styles through geologic era: Hadean tectonics, Archaean Tectonics, Stagnant to Mobile-Lid tectonics and the present-day Modern tectonics in Earth's history (modified from Gerya, 2019). c) Representative diagram of their geodynamic mechanisms: i) RTI assisted lithospheric drips, ii) convective dripping, and iii) detachment driven delamination (modified after McMillan & Schoenbohm, 2023).

Figure 2. a) Initial model set-up and associated boundary conditions used for CFD simulations of RTI assisted lithospheric dripping. All the walls of the domain are assigned free-slip boundary conditions. Density perturbations are introduced within lithosphere as a consequence of eclogitization, within are either sinusoidal or random in nature (see inset). The top and bottom temperatures are maintained at 300 K and 4400 K respectively. b) The depth profiles for initial (i) density, (ii) temperature and (iii) viscosity, maintained at onset of our simulations in the model domain.

Figure 3. a) Onset of dripping process at the lithospheric base by Rayleigh-Taylor instability in a model. b) Three principal mechanisms of dripping recognized from model simulations: formation of axisymmetric superdrip (i), development of asymmetric drips followed by their stagnation at the mid-mantle transition (ii), and iii) growth of asymmetric keels at the lithospheric base.

Figure 4: Progressive growth of lithospheric drips via three principal mechanisms in CFD model simulations. Reference experiments run with three different sets of conditions a) B = 0.79 and $\Delta\rho_{MM}$ = 200 kg/m^3 and M =10; b) B = 0.48 and $\Delta\rho_{MM}$ = 100 kg/m^3 and M = 10, and c) B = 0.09, $\Delta\rho_{MM}$ = 100 kg/m^3 and M= 10. White contours originating from CMB demarcate plume-related isotherms(2020 K, 2100 K, 2200 K) Note the formation of superdrip structure in (a iii-iv), mid-mantle stagnation of the drips in (b-iii), lithospheric keels in (c - iii). Note. Here 1 Ma = 1 Myr = 1 million years.

Figure 5: Graphical plots of a) heat flux and b) mean velocity as a function of time during the evolution of the three reference models shown in Figure 4. c) Comparison of horizontal/vertical mantle flow velocity ratios for both upper and lower mantle in the reference experiments. d) Difference in velocity for a single solitary drip and super drips in mechanism 1 reference experiments. e) A comparative analysis of the rate of lithospheric erosion and total reduction in lithosphere volume with time for the three reference experiments.

Figure 6: Variations in dripping velocity and drip growth rate (a) , and heat flux (b) with the buoyancy number B. (c) Time series analysis of the ratio between horizontal and vertical velocity components (v_x/v_z), characterizing mantle flow for the three principal mechanisms of lithospheric dripping for both upper and lower mantle.

Figure 7: Fields of the lithospheric dripping mechanisms in a parametric space defined by $\Delta\rho_{base}$ (density changes at the crustal base, $\Delta\rho_{base} = \Delta\rho_p + \Delta\rho_{CB}$) and $\Delta\rho_{MM}$ (mid-mantle density changes due to eclogitization), buoyancy numbers B and B_{MM} (dependant on $\Delta\rho_{MM}$)

Figure 8: a) A correlation between the mantle flow velocity patterns produced by the dripping mechanisms: 1, 2 and 3 and b) their corresponding thermal structures (isotherms for drips in mechanism 1: 1850, 1980 K, mechanism 2: 1850, 1950, 2000 K, mechanism 3: 1650, 1800, 1950 K). Notice that the temperatures (1650 - 1950 K) are redistributed in the lower mantle most effectively by mechanism 3.

Figure 9: a) Global distribution of the present-day lithospheric dripping regions (modified after McMillan & Schoenbohm, 2023). b) Seismic sections (lower panels) showing dripping configurations in mantle beneath (i) Southern Puna and Arrizaro (modified after Calixto et al., 2013), (ii) Southeast Carpathians and Vrancea (modified from Ren et al., 2012), (iii) Colorado Plateau and Grand Canyon(modified from Levander et al., 2011), (iv) Central Anatolian plateau(modified from Andersen et al., 2024), (v) Hindu Kush (modified after Koulakov, 2011) and (vi) Isabella basin in Great Valley, California (modified after Cox et al., 2016).

Figure 10: A conceptual cartoon depicting the Earth's early geodynamic evolution in the perspective of the three dripping mechanisms recognized in the present study (modified from Rolf et al., 2022).

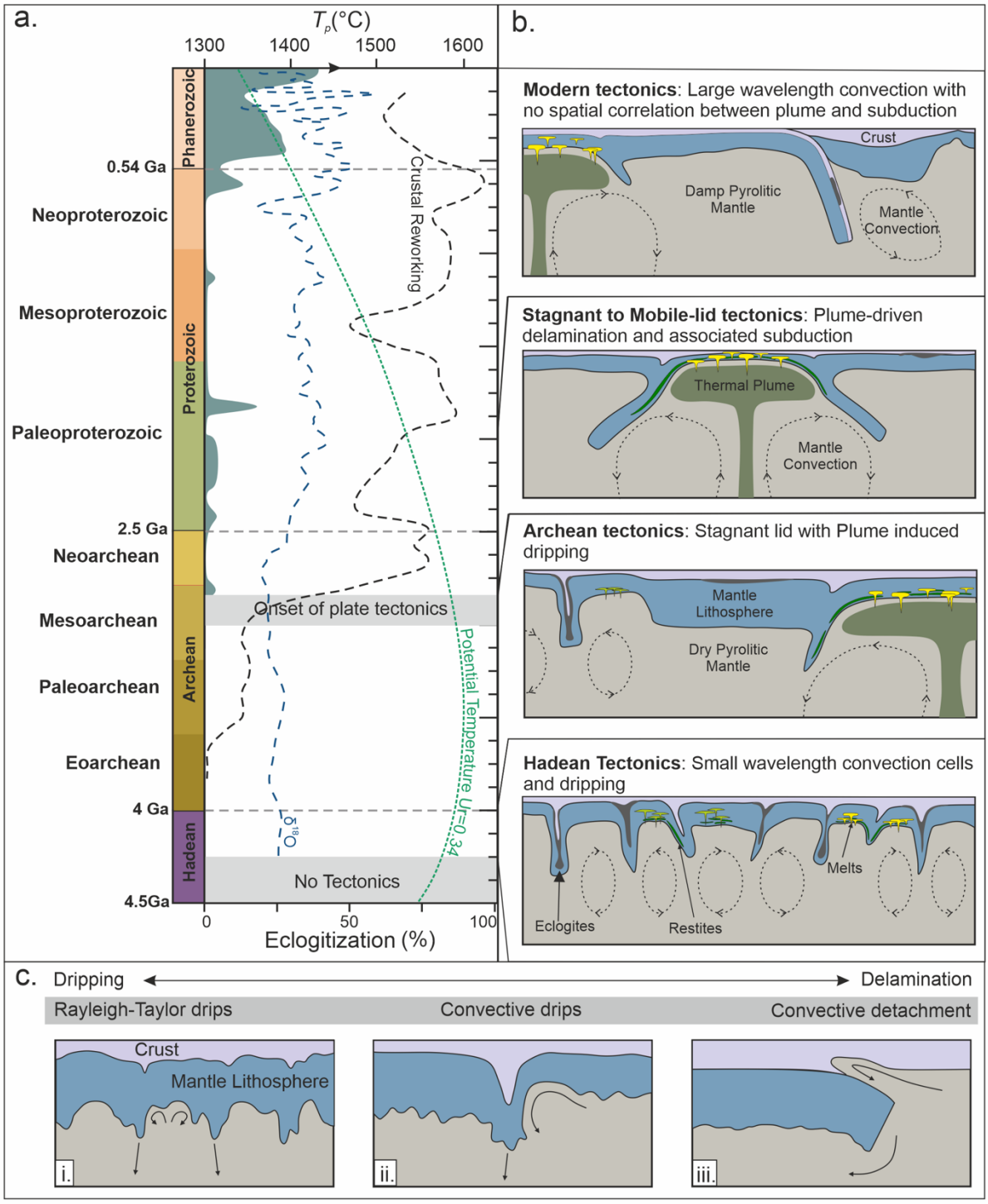
a.
T_p(°C)
1300
1400
1500
1600
Phanerozoic
Proterozoic
Archean
Hadean
0.54 Ga
Neoproterozoic
Mesoproterozoic
Paleoproterozoic
2.5 Ga
Neoarchean
Mesoarchean
Paleoarchean
Eoarchean
4 Ga
4.5Ga
Crustal Reworking
Onset of plate tectonics
Potential Temperature U=0.34
$\delta^{18}O$
No Tectonics
0
50
100
Eclogitization (%)
b.
Modern tectonics: Large wavelength convection with no spatial correlation between plume and subduction
Crust
Damp Pyrolitic Mantle
Mantle Convection
Stagnant to Mobile-lid tectonics: Plume-driven delamination and associated subduction
Thermal Plume
Mantle Convection
Archean tectonics: Stagnant lid with Plume induced dripping
Mantle Lithosphere
Dry Pyrolitic Mantle
Hadean Tectonics: Small wavelength convection cells and dripping
Melts
Eclogites
Restites
c.
Dripping
Delamination
Rayleigh-Taylor drips
Convective drips
Convective detachment
Crust
Mantle Lithosphere
i.
ii.
iii.

Figure 1

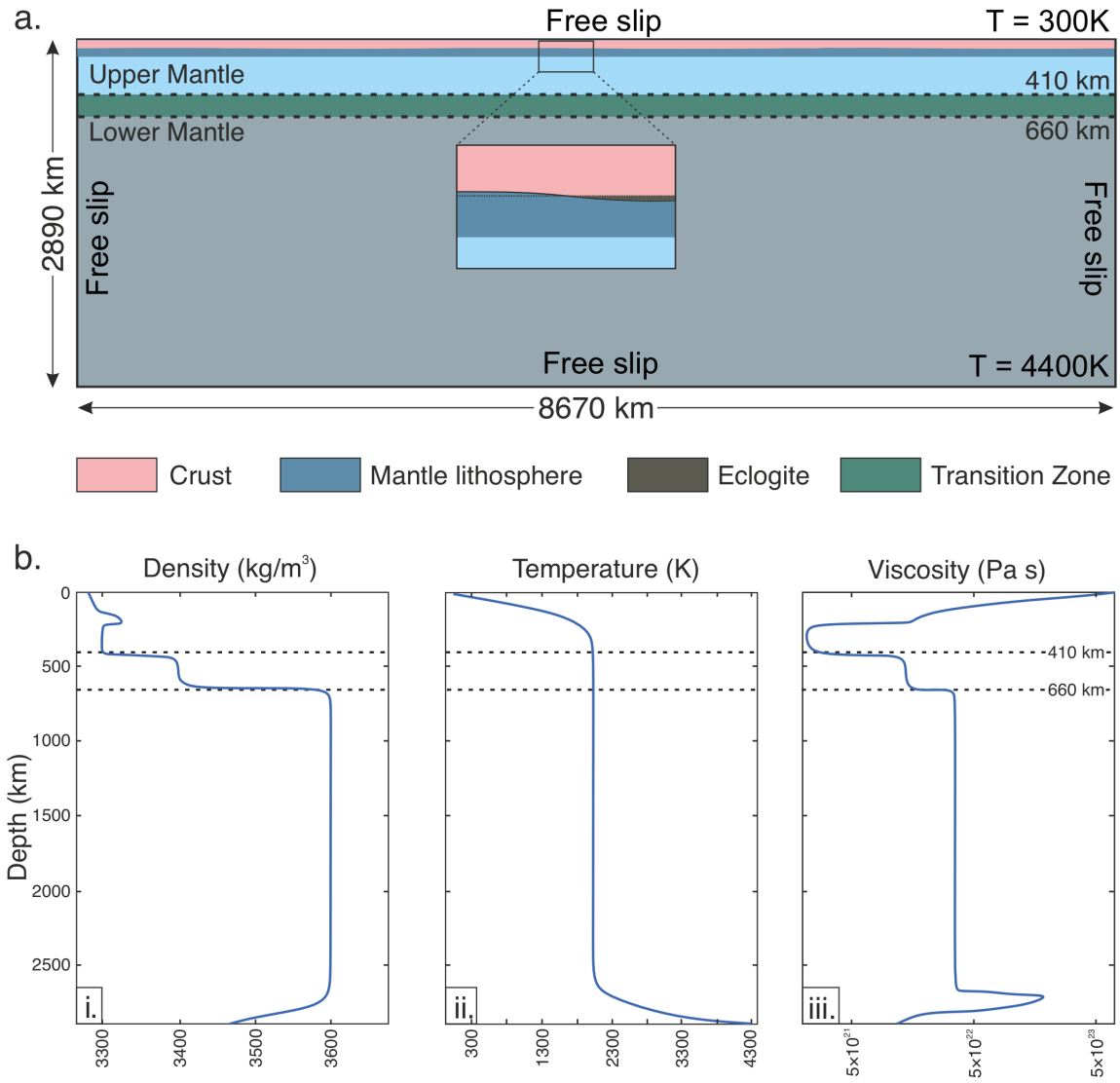
a.
Free slip
T = 300K
Upper Mantle
410 km
Lower Mantle
660 km
2890 km
Free slip
Free slip
Free slip
T = 4400K
8670 km
Crust
Mantle lithosphere
Eclogite
Transition Zone
b.
Density (kg/m3)
Temperature (K)
Viscosity (Pa s)
Depth (km)
0
500
1000
1500
2000
2500
410 km
660 km
i.
ii.
iii.
3300
3400
3500
3600
300
1300
2300
3300
4300
5×10^21
5×10^22
5×10^23

Figure 2

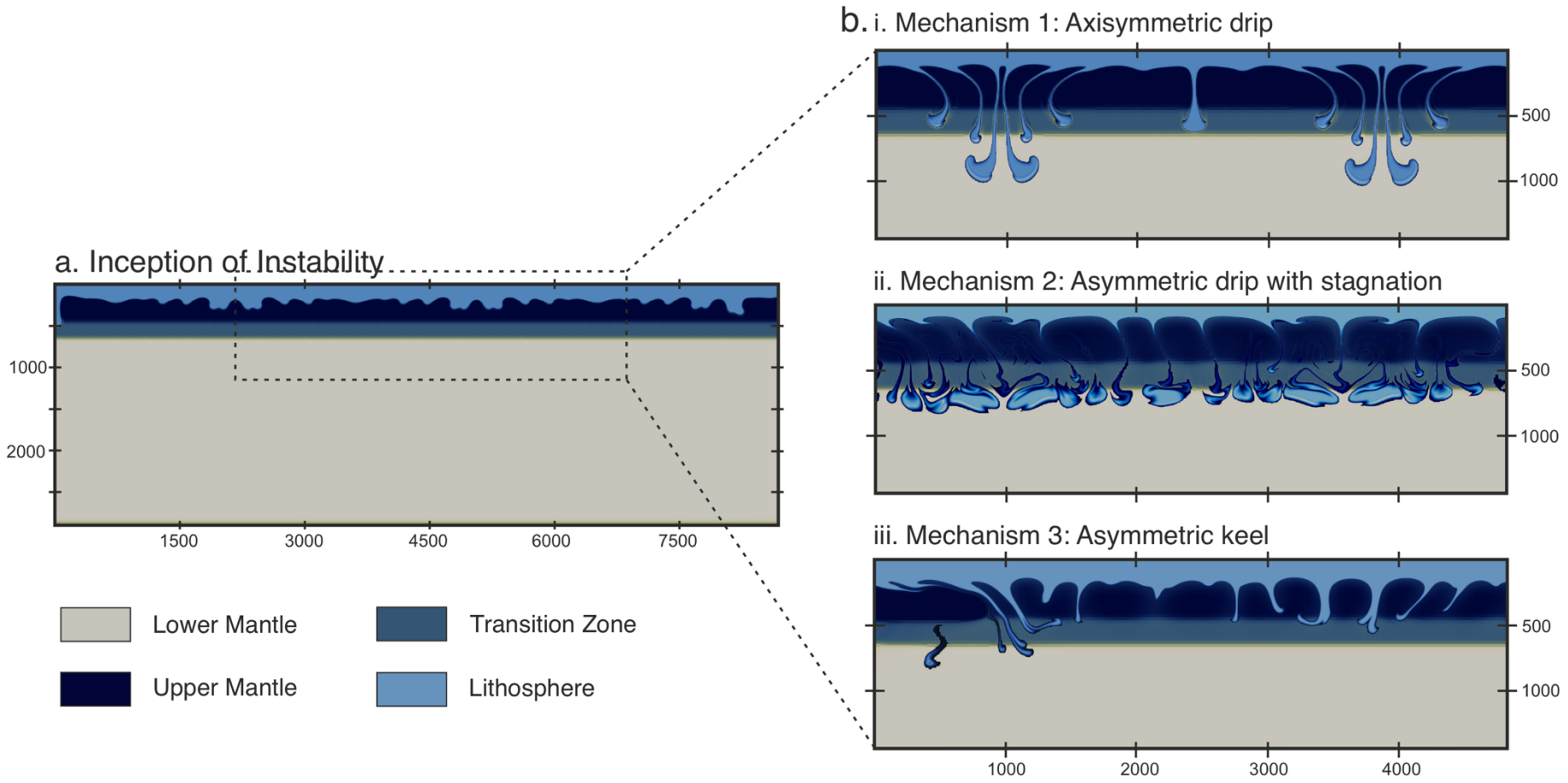
a. Inception of Instability
1000
2000
1500
3000
4500
6000
7500
b. i. Mechanism 1: Axisymmetric drip
500
1000
ii. Mechanism 2: Asymmetric drip with stagnation
500
1000
iii. Mechanism 3: Asymmetric keel
500
1000
1000
2000
3000
4000
Lower Mantle
Transition Zone
Upper Mantle
Lithosphere

Figure 3

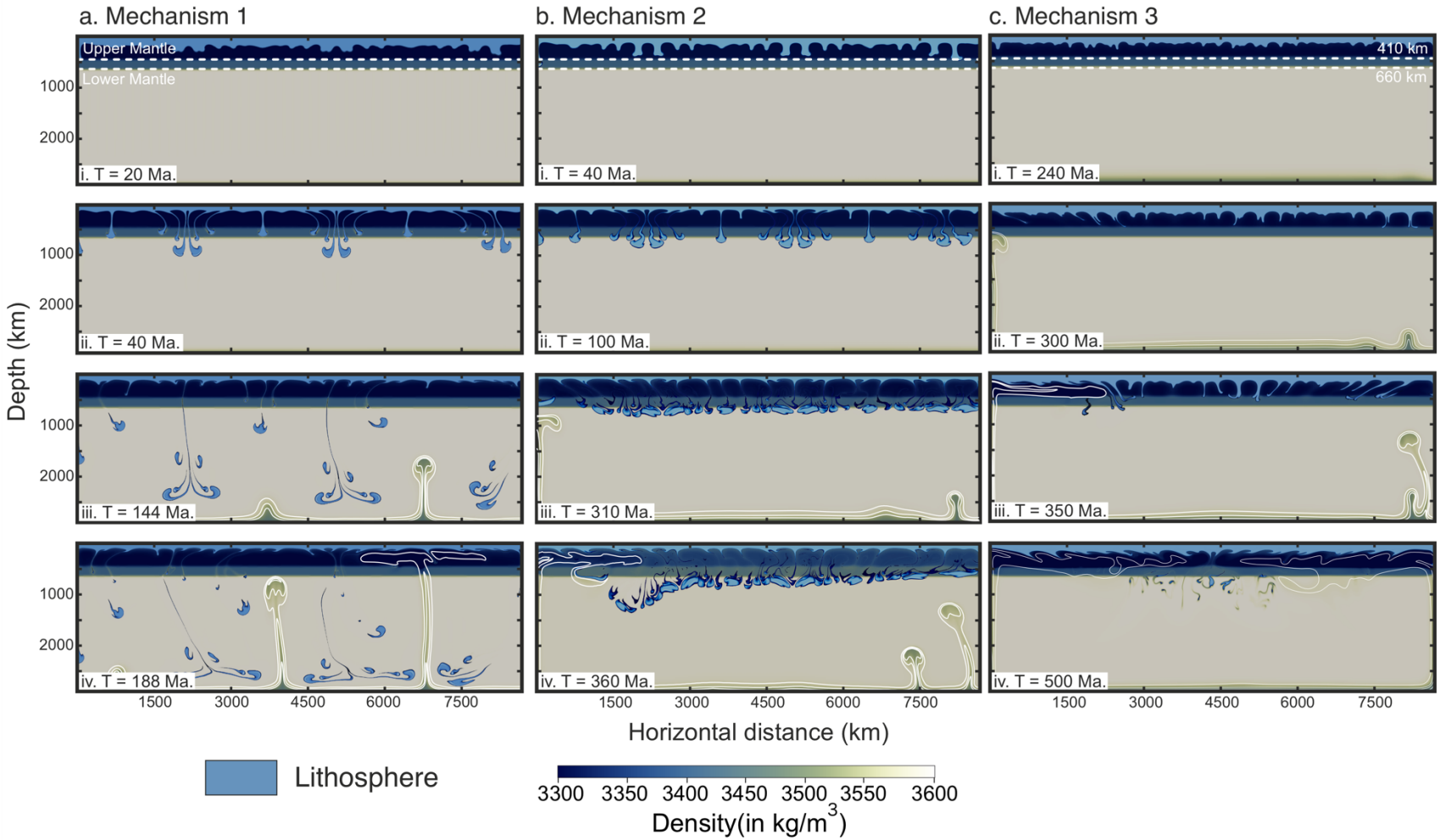
a. Mechanism 1
b. Mechanism 2
c. Mechanism 3
Upper Mantle
Lower Mantle
410 km
660 km
Depth (km)
1000
2000
i. T = 20 Ma.
i. T = 40 Ma.
i. T = 240 Ma.
ii. T = 40 Ma.
ii. T = 100 Ma.
ii. T = 300 Ma.
iii. T = 144 Ma.
iii. T = 310 Ma.
iii. T = 350 Ma.
iv. T = 188 Ma.
iv. T = 360 Ma.
iv. T = 500 Ma.
1500
3000
4500
6000
7500
Horizontal distance (km)
Lithosphere
3300 3350 3400 3450 3500 3550 3600
Density(in kg/m3)

Figure 4

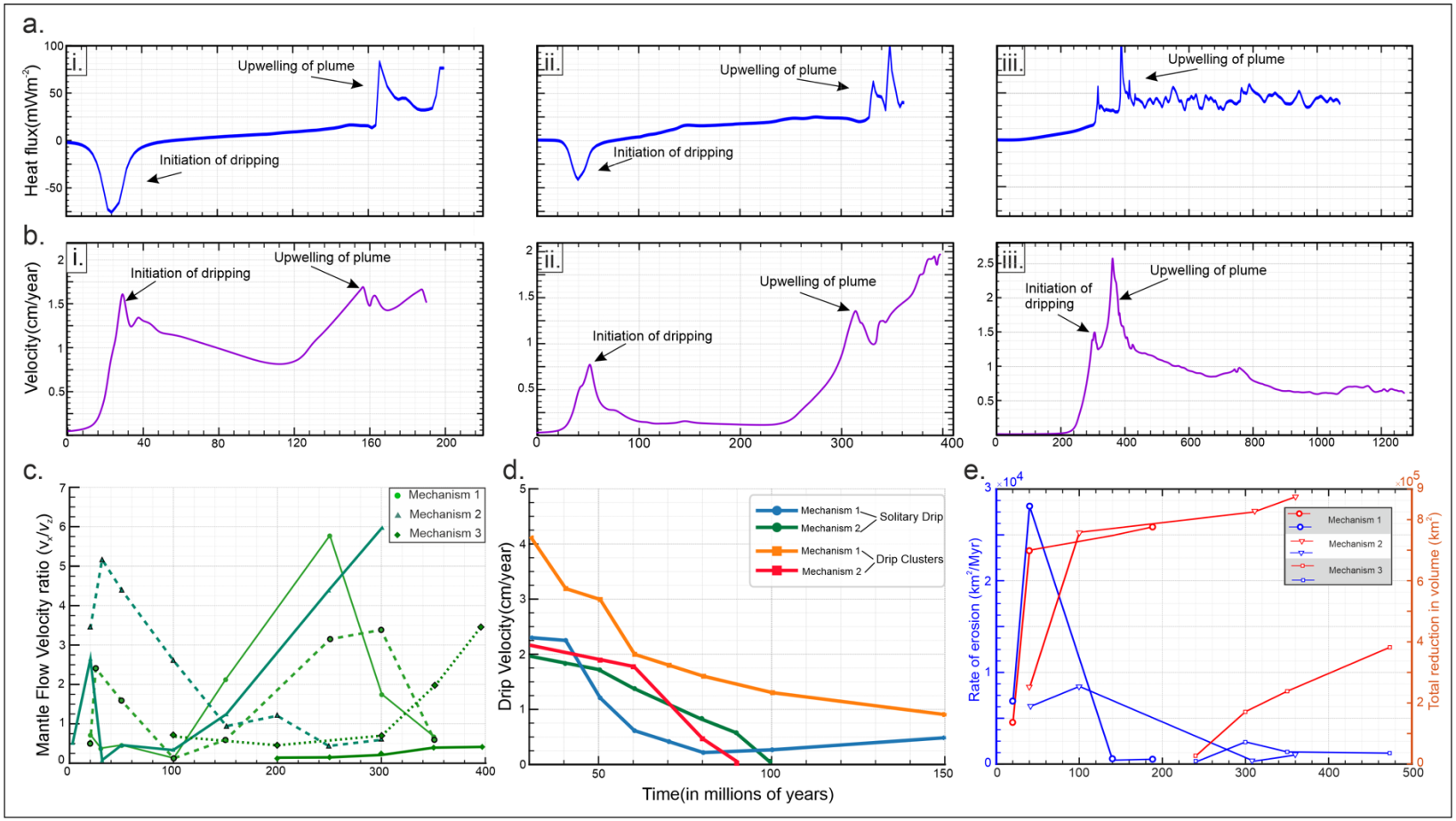
a.
i.
ii.
iii.
Heat flux(mWm-2)
Upwelling of plume
Initiation of dripping
b.
Velocity(cm/year)
c.
Mantle Flow Velocity ratio (vx/vz)
Mechanism 1
Mechanism 2
Mechanism 3
d.
Drip Velocity(cm/year)
Solitary Drip
Drip Clusters
Time(in millions of years)
e.
Rate of erosion (km2/Myr)
Total reduction in volume (km3)

Figure 5

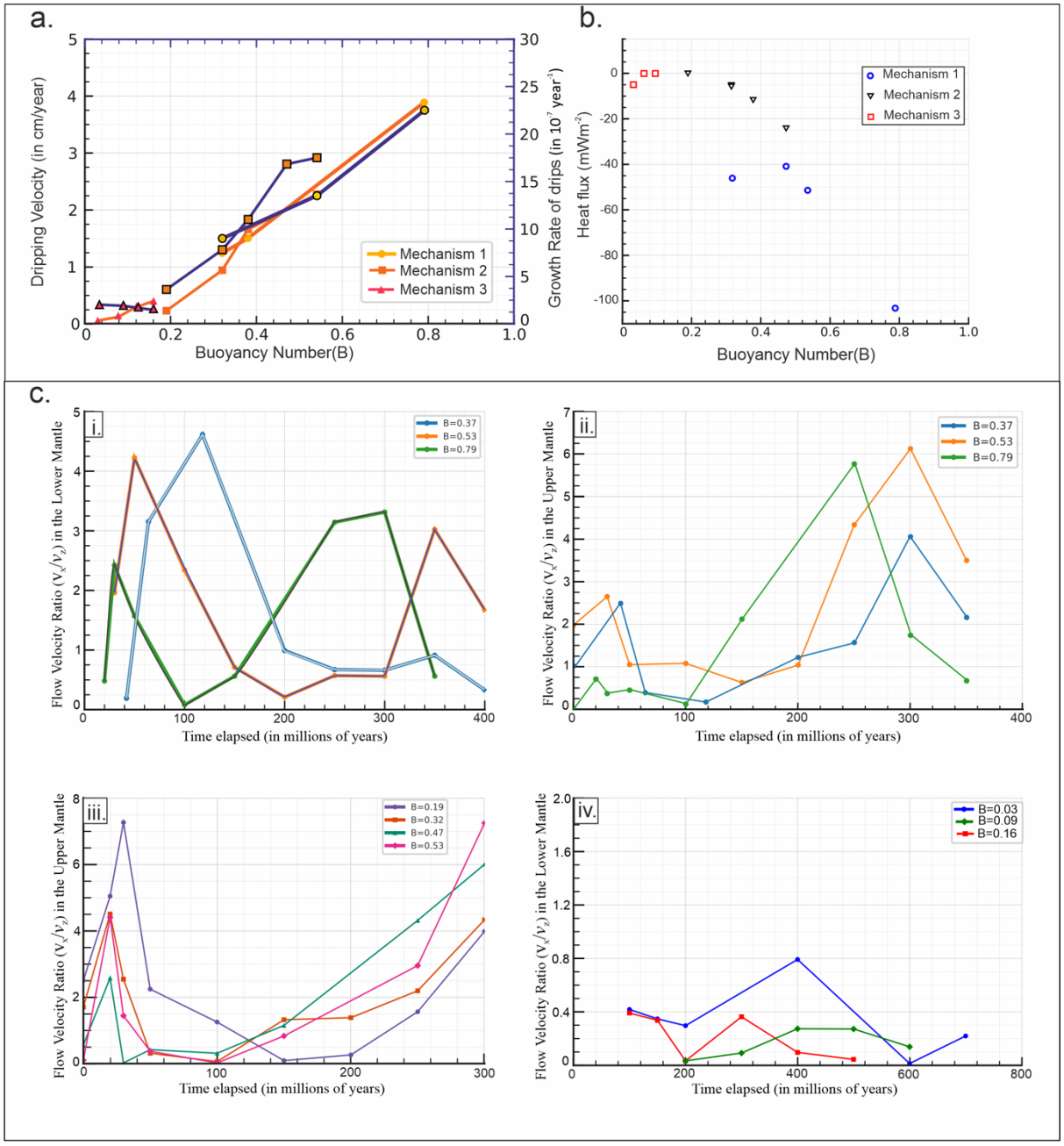
a.
Dripping Velocity (in cm/year)
Growth Rate of drips (in 10^-7 year^-1)
Buoyancy Number(B)
Mechanism 1
Mechanism 2
Mechanism 3
b.
Heat flux (mWm^-2)
Buoyancy Number(B)
Mechanism 1
Mechanism 2
Mechanism 3
c.
i.
Flow Velocity Ratio (Vx/Vz) in the Lower Mantle
Time elapsed (in millions of years)
B=0.37
B=0.53
B=0.79
ii.
Flow Velocity Ratio (Vx/Vz) in the Upper Mantle
Time elapsed (in millions of years)
B=0.37
B=0.53
B=0.79
iii.
Flow Velocity Ratio (Vx/Vz) in the Upper Mantle
Time elapsed (in millions of years)
B=0.19
B=0.32
B=0.47
B=0.53
iv.
Flow Velocity Ratio (Vx/Vz) in the Lower Mantle
Time elapsed (in millions of years)
B=0.03
B=0.09
B=0.16

Figure 6

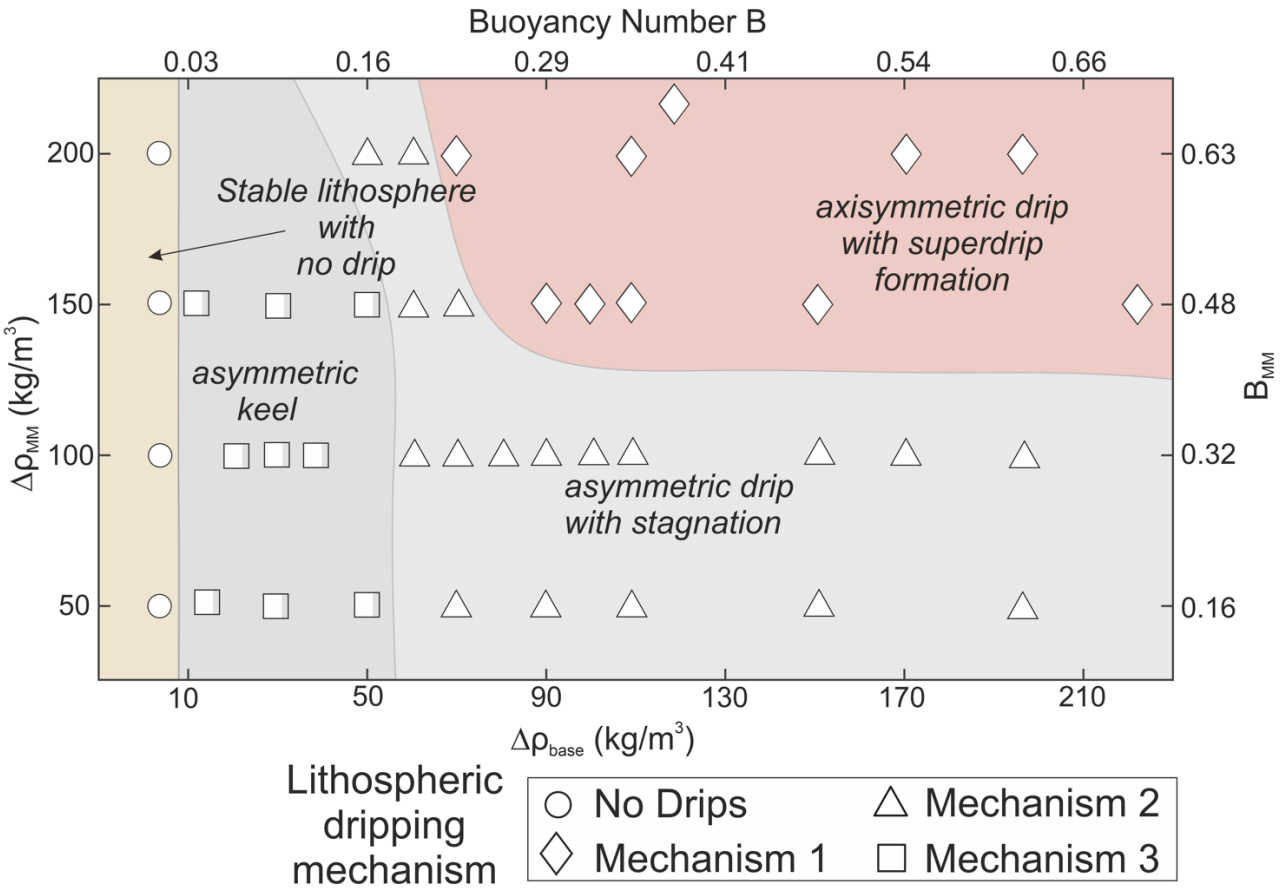
Buoyancy Number B
0.03
0.16
0.29
0.41
0.54
0.66
200
150
100
50
0.63
0.48
0.32
0.16
$\Delta\rho_{MM}$ (kg/m^3)
B_{MM}
Stable lithosphere with no drip
axisymmetric drip with superdrip formation
asymmetric keel
asymmetric drip with stagnation
10
50
90
130
170
210
$\Delta\rho_{base}$ (kg/m^3)
Lithospheric dripping mechanism
No Drips
Mechanism 1
Mechanism 2
Mechanism 3

Figure 7

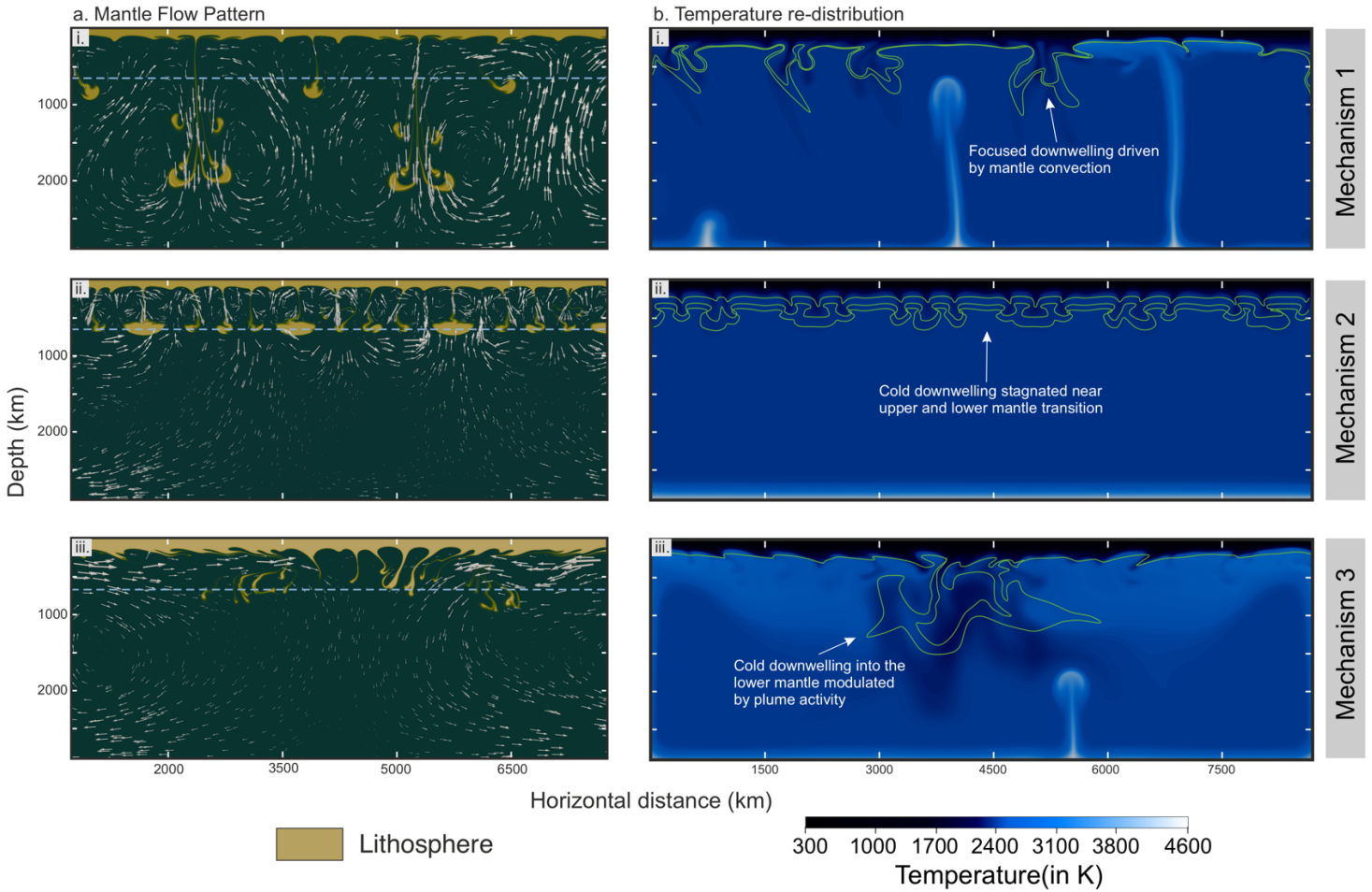
a. Mantle Flow Pattern
b. Temperature re-distribution
i.
ii.
iii.
1000
2000
Depth (km)
Focused downwelling driven by mantle convection
Cold downwelling stagnated near upper and lower mantle transition
Cold downwelling into the lower mantle modulated by plume activity
Mechanism 1
Mechanism 2
Mechanism 3
2000
3500
5000
6500
1500
3000
4500
6000
7500
Horizontal distance (km)
Lithosphere
300 1000 1700 2400 3100 3800 4600
Temperature(in K)

Figure 8

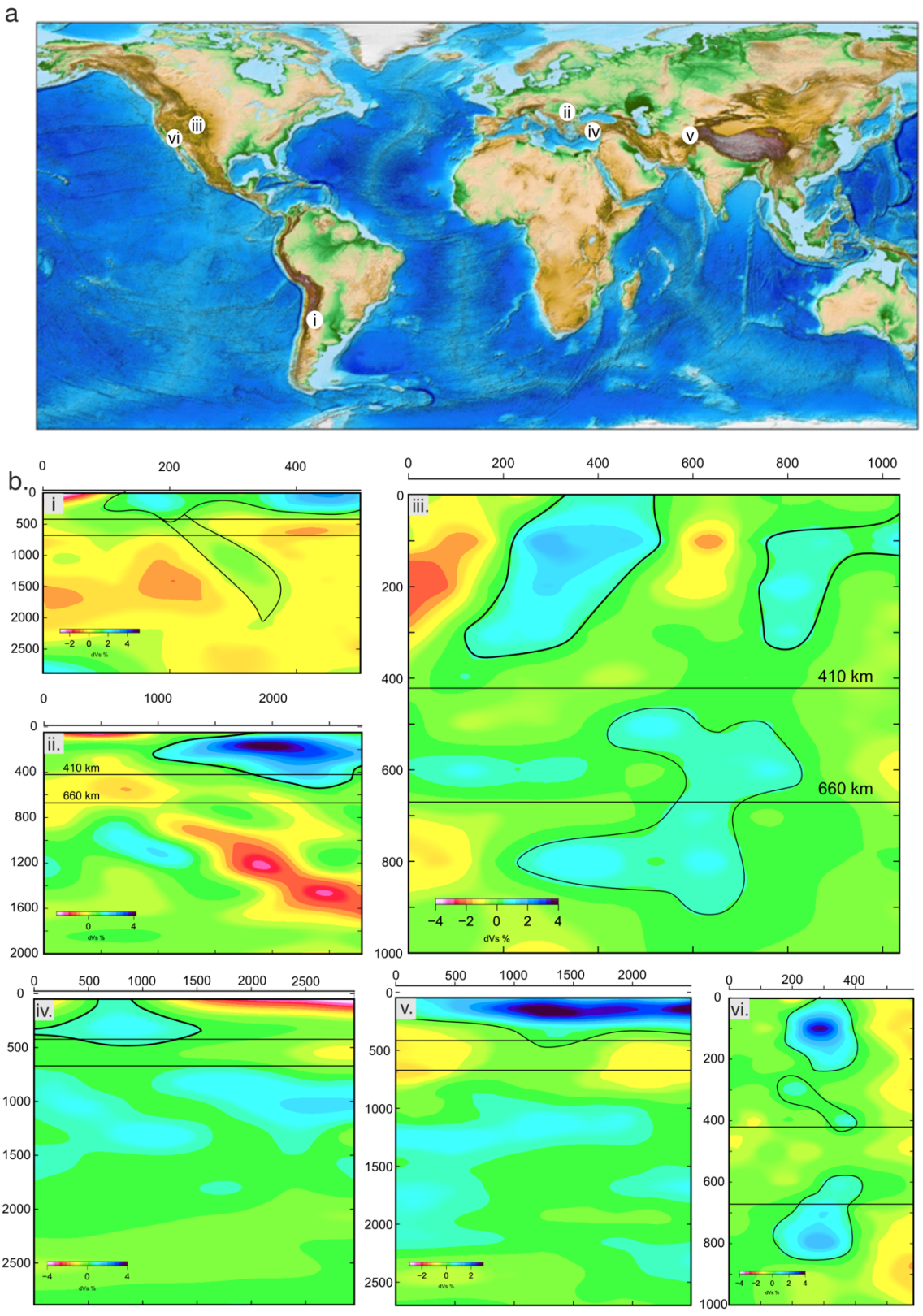

Figure 9

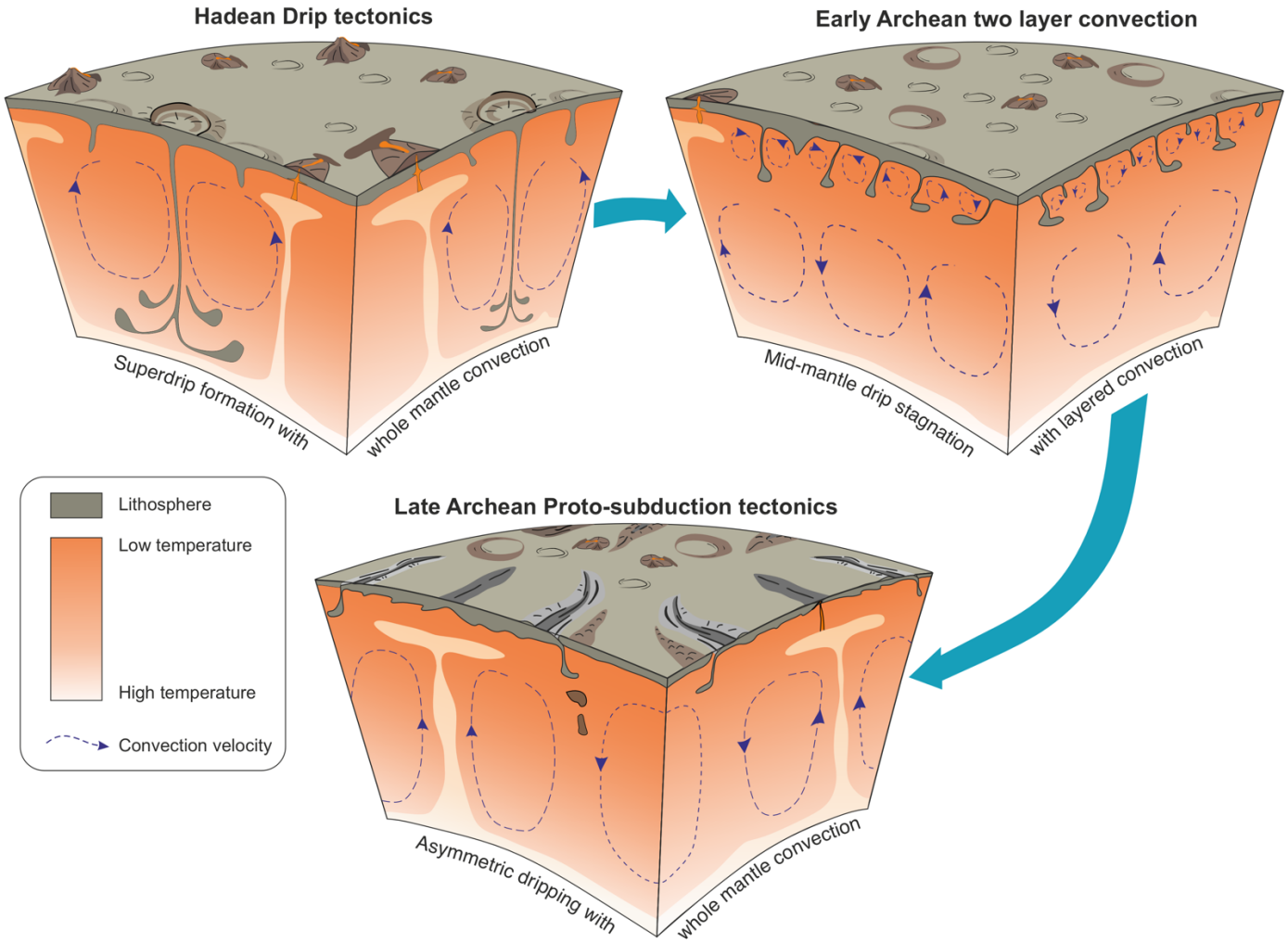
Hadean Drip tectonics
Superdrip formation with
whole mantle convection
Early Archean two layer convection
Mid-mantle drip stagnation
with layered convection
Late Archean Proto-subduction tectonics
Asymmetric dripping with
whole mantle convection
Lithosphere
Low temperature
High temperature
Convection velocity

Figure 10

Table 1

Model Parameters	Values
lithosphere thickness z_0	200 km
Reference density ρ_0	3300 kg/m³
Reference viscosity μ_0	2×10^{21} Pa s
Lower mantle viscosity	6×10^{22} Pa s
Lithosphere viscosity	$2 \times 10^{22} – 10^{24}$ Pa s
Compositional viscosity pre-factor $\zeta(C)$	10-1000
Thermal conductivity k*	4.7 W K^{-1} m^{-1}
Specific heat C_p	1250 J K^{-1} kg^{-1}
Thermal expansivity α_0	3×10^{-5} K^{-1}
Top temperature T_{top}	300 K
Bottom temperature T_{bot}	4400 K
Reference Temperature T_0	1600 K
Reference Rayleigh number Ra	5×10^7
Background Heating rate X	6×10^{-9} W/m³
Clapeyron slope at 660 km phase transition γ_{660} #	-2×10^6 Pa/K
Density change at 660 km phase transition (Ambient Mantle) **	200 kg/m³
Clapeyron slope at 410 km phase transition γ_{410} #	3×10^6 Pa/K
Density change at 410 km phase transition (Ambient Mantle) **	100 kg/m³

* Thermal diffusivity (κ_0) is calculated in ASPECT from thermal conductivity and it has a value of 10^{-6}

Taken from Katsura, T., et al., (2004)

** Taken from J. Ganguly et al., (2009)

Table 2

Parameter	Values
Drip perturbation density difference $\Delta\rho_P$	(-100) - 50 kg/m³
Viscosity ratio M†	10 - 1000
Buoyancy number B	0 - 0.9
Density change due to eclogitization at the base of the thickened crust $\Delta\rho_{CB}$	10 - 200 kg/m³
$\Delta\rho_{base}$	0 - 250 kg/m³
Density change due to eclogitization at the mantle transition zone $\Delta\rho_{MM}$	10 - 220 kg/m³
Density change due to eclogitization $\Delta\rho_E$ $(= \Delta\rho_{CB} + \Delta\rho_{MM})$	100 - 350 kg/m³

† Ratio of viscosity of the dripping lithosphere and the ambient mantle